Meteoritic Matter and Spherules in a Presumed Impact Crater at Emmerting, Germany

Václav Procházka , Pavel Kalenda , Petr Martinec , Jiří Mizera * , Lenka Thinová , Tomáš Trojek , Günther Kletetschka , Richard Štorc , Jan Adámek , Pavel Švanda

Posted Date: 26 March 2024

doi: 10.20944/preprints202403.1621.v1

Keywords: impact crater; meteorite; enstatite; Mg-rich glass; Fe oxide spherules

Article

Meteoritic Matter and Spherules in a Presumed Impact Crater at Emmerting, Germany

Václav Procházka [1], Pavel Kalenda [2], Petr Martinec [3], Jiří Mizera [4,*], Lenka Thinová [1], Tomáš Trojek [1], Günther Kletetschka [5,6], Richard Štorc [5], Jan Adámek [1] and Pavel Švanda [7]

[1] Faculty of Nuclear Sciences and Physical Engineering, Czech Technical University in Prague, Břehová 7, Praha 1, 11519, Czech Republic; vaclav.prochazka@fjfi.cvut.cz (V.P.); tomas.trojek@fjfi.cvut.cz (T.T.); lenka.thinova@fjfi.cvut.cz (L.T.); jan.adamek@fjfi.cvut.cz (J.A.)
[2] CoalExp, Pražmo 129, 73904 Czech Republic; p.kalenda@volny.cz
[3] Czech Academy of Sciences, Institute of Geonics, Studentská 1768, Ostrava-Poruba, 70800, Czech Republic; martinec@ugn.cas.cz (P.M.)
[4] Czech Academy of Sciences, Nuclear Physics Institute, Husinec-Řež 130, 25068, Czech Republic
[5] Faculty of Science, Charles University in Prague, Albertov 6, Praha 2, 12843, Czech Republic; gunther.kletetschka@natur.cuni.cz (G.K.); richard.storc@natur.cuni.cz (R.Š.)
[6] Geophysical Institute, University of Alaska-Fairbanks, 2156 N Koyukuk Drive, Fairbanks, AK 99775, USA
[7] University of Pardubice, Studentská 95, 530 09 Pardubice, Czech Republic, pavel.svanda@upce.cz
* Correspondence: mizera@ujf.cas.cz

Abstract: Bulk composition, mineralogy and microchemistry of various fractions of the filling of the Crater No. 4 at Emmerting were investigated. Here we present mainly the fine fractions, which, in contrast to pebbles larger than ca. 4 cm, are relatively poor in material affected by melting. A 0.1 mm long meteorite fragment without ablation features was found, and remelted fragments of the same body have been identified. The projectile was dominated by enstatite, also containing forsterite, basic plagioclase, Ni-rich pyrrhotite and troilite, kamacite, silica, and probably merrillite. The molten fragments contain porous Mg-rich glass (indicating temperature > 1500 °C), minor Fe oxides, and occasionally uncommon Ni-rich minerals. The bulk composition and electron microprobe show that the amount of meteoritic material is low (<< 1 %), and it is not unequivocally manifested even in platinum-group elements abundances and osmium isotope ratios (the latter, however, were only measured in two samples). This can be explained by dilution of the filling by particles brought after the crater formation, and by probably achondritic composition of the projectile. Relatively large hollow spheroid Fe oxide particles were observed in thin sections from the magnetic fraction. A Mn oxide hollow spherule has also been found. In magnetically separated filling from the nearby Crater No. 5, bulk chemical composition points to contamination with several metals and metalloids probably due to influence of recent alluvial sediments. Therefore, the extent of meteoritic contamination in this crater may be even smaller.

Keywords: impact crater; meteorite; enstatite; Mg-rich glass; Fe oxide spherules

1. Introduction

Small impact craters are prevalently formed in porous and relatively loose rocks where the most of energy is transformed to heat at the expense of diagnostic shock effects ([1] and references therein). Melting and high-temperature (HT) metamorphism are usually not unequivocal proofs of impact [2]. On the other hand, the inhomogeneity of a porous target leads to greater variability of the shock pressure, which is generally smaller than in compact rocks but can be locally significantly enhanced, producing varied shock phenomena and melting at the microscale [3].

Shock metamorphism has also been proven in small impact craters: it was significant even in the Kamil crater with a diameter of 45 m [4]. In the Carancas crater with a 13.5 m diameter (i.e., comparable to the craters at Emmerting presented in this work), small-scale melting of the projectile

 doi:10.20944/preprints202403.1621.v1

with melt injections into the target sediments was documented and weak shock effects were found in the ejecta [5]. Thus, the shock effects could be, in principle, found even in very small impact craters, but in such a case the shocked material usually has small volume and is dispersed in relatively large area. Thus, findings of meteoritic iron have been the main evidence for impact origin of small craters [1]. The most important exception is the witnessed fall of the Carancas meteorite in 2007, which has proven that even small stone meteoroids may reach the surface with the velocity of several km/s [5]. In older craters, however, the stone meteorite relics decayed to such extent that they cannot be macroscopically identified; hundreds of years are sufficient for almost complete decay in humid climate [6].

The two impact craters at Emmerting investigated (Nos. 4 and 5 in the numbering of suspect depressions near Burghausen – see [7]) have formed in very coarse unconsolidated sediments of Quaternary alluvial terraces. No impact crater in a similar target has widely been accepted yet [1]. First geological, geophysical and petrographic indices for impact origin of the Crater No. 4 were presented mainly in a report [8] and a conference paper [9]. Claims of the anthropogenic origin of the depressions with molten rocks in the region, e.g., a comparison to ruins of old limekilns [10,11] were presented as an opposition against the "Chiemgau Impact" theory with no particular reference to Emmerting [12]. In conference contributions [13,14] and in our companion paper [15], we have presented the HT effects and deformation of pebbles in the crater, and showed that human activities are unable to explain the HT and deformation effects. The same holds for the nearby Crater No. 5 which, however, has been investigated less intensely.

In this paper, the bulk material balance is discussed, and results of investigation of the meteoritic material found are presented. Another recent paper [16] presents geophysical results which are also consistent with the impact origin of the craters.

2. Material and Methods

2.1. Sample Sorting and Separation

In the companion paper [15], we have documented the coarse fraction of the filling, i.e., pebbles or large fragments with sizes ranging from 4 cm to >20 cm, which often have glass coatings and other unusual features. Here we present the remaining fractions. Samples were gathered to represent various depths not exceeding 40–50 cm below the recent crater floors. The gravel from Crater No. 4 was cleaned from plant biomass, washed and chemically analyzed. However, most effort has been dedicated to fine fractions where a better chance to find meteoritic matter was expected. See also Figure 1 for the overview of fractions separated and analytical methods applied.

The fractions < 2 mm from the Crater No. 4 were obtained in two different ways. In the first case, combination of sieving and washing of the loam from the small pebbles (gravel) with distilled water was applied. This material was separated in a suspension in distilled water using a strong permanent neodymium magnet. After drying, the magnetic fraction (MFa, also used in search for meteoritic material) constituted 1 wt.% of the fine fraction, a transitional, slightly magnetic fraction (SMF) 0.5 wt.%, and the non-magnetic fraction (NFa) made up 98.5 wt.%. Another aliquot of the filling (< 2 mm) was separated by sieving and electromagnetically. The material was desiltered using a sieve with the mesh size 0.063 mm in distilled water. Then, the oversize fraction was dried and separated into 5 size fractions (using mesh sizes 0.1, 0.25, 0.5 and 1 mm). These fractions were examined with stereomicroscope and then separated electromagnetically (with maximum magnetic field intensity). For closer investigation, the magnetically separated fractions with grain size 0.063 – 1 mm (MFb1, NFb1) and 0.1 – 0.25 mm (MFb2, NFb2) were selected.

Polished thin-sections for petrographic microscopy and SEM with standard thickness (30 μm) were made from MFa, MFb1 and NFb1. In addition, a thick section was made from MFa which is better for preservation of larger grains (up to 2 mm) than the thin section.

From Crater No. 5, only separation with a permanent magnet from suspension (again combining sieved and washed material < 2 mm) was applied (in the same way as from the Crater No. 4).

 doi:10.20944/preprints202403.1621.v1

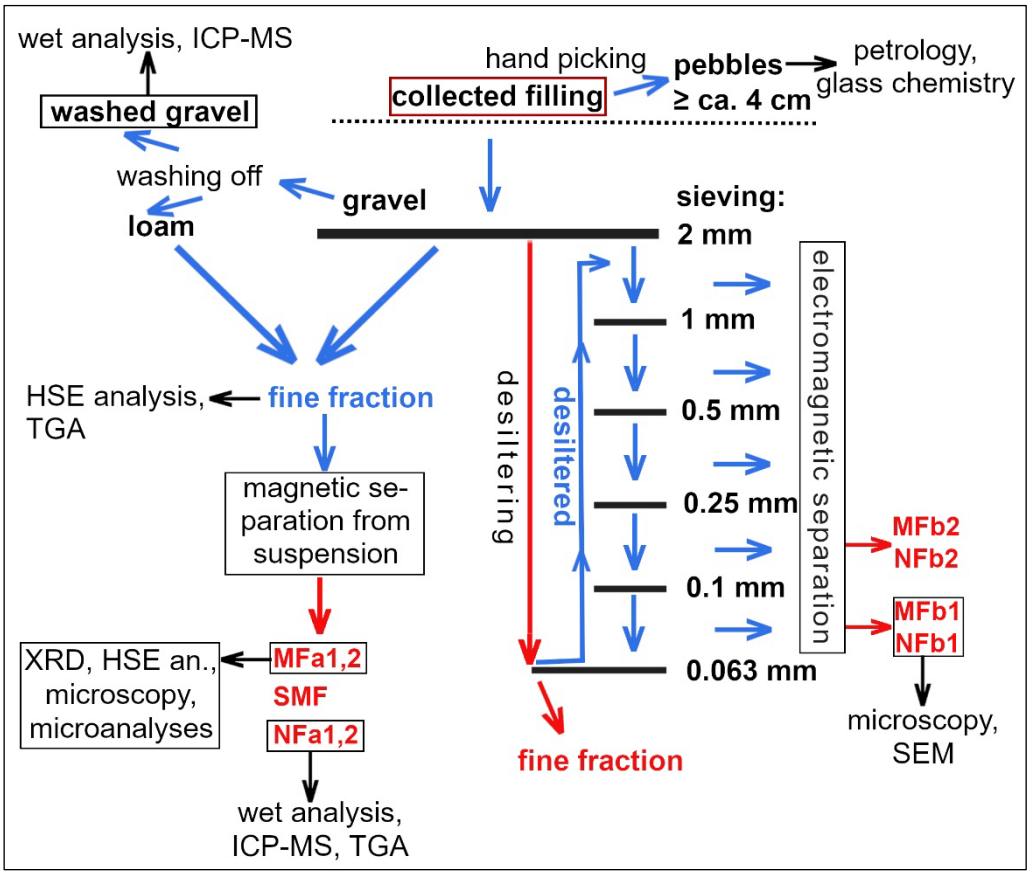

Figure 1. Scheme of processing of the filling of Crater No. 4 and analytical methods applied. The samples used for INAA are indicated in red.

2.2. Bulk Chemical Analyses

2.2.1. Chemical Whole Rock and ICP-MS Analyses

Pebbles with usually 1–3 cm in size, washed in distilled water, were pulverized and analyzed using the wet chemical whole rock analysis and Inductively Coupled Plasma Mass Spectrometry (ICP-MS) after acidic decomposition (alkaline fusion prior to dissolution was not applied). For the ICP-MS analytical protocol, see [17]. In addition, one sample of NFa was analyzed by the same procedure.

2.2.2. Thermogravimetric Analysis (TGA)

The weight loss was examined for temperatures of 100, 150, 200, 250, 300, 400, 500, 600, 700, 800, and 1000 °C. Homogenized duplicate samples were heated to respective temperatures for 2 hours.

2.2.3. Instrumental Neutron Activation Analysis (INAA)

Homogenized samples of selected fractions and manually separated glasses were analyzed for elemental composition using INAA. Long-time (LT) irradiation mode (mainly for trace elements and Na, K, and Fe) was applied for all samples, and for the samples MFa, NFa (both duplicated) and SMF also short-time (ST) irradiation mode was used (for most of the major elements and some trace elements). The LVR-15 nuclear reactor within the CANAM and CICRR infrastructures (Řež, Czech Republic) was employed. For details on INAA procedures including associated uncertainties, possible interferences, etc., see [18–20]. Reference materials were analyzed with samples: the USGS GSP-2 (granodiorite) in ST irradiation, and CRPG GS-N (granite) in LT irradiation. The bulk composition of the whole fraction < 2mm was calculated as weighted average of MFa, NFa and SMF

 doi:10.20944/preprints202403.1621.v1

(and in the same way in Crater No. 5). Glasses were taken from a large pebble from the Crater No. 4. For comparison, one sample of glass coating on an orthogneiss pebble was added from the Kaltenbach structure, and one glass coating sample from an old limekiln at Frechensee, Seeshaupt (see also [15]).

2.2.4. Analyses of Highly Siderophile Elements (HSE) and Os Isotope Ratios

Concentrations of platinum-group elements (PGE) (except for Rh) and Re, and the $^{187}Os/^{188}Os$ isotope ratios were measured in the laboratory of the Institute of Geology of the Czech Academy of Sciences using the methods outlined in detail in [21]. Samples were dissolved and equilibrated with a mixed ^{185}Re-^{190}Os and ^{191}Ir–^{99}Ru–^{105}Pd–^{194}Pt spikes using Carius Tubes and reverse *aqua regia*. The decomposition was followed by Os separation through solvent extraction by $CHCl_3$ and Os microdistillation. The elements Ir, Ru, Pt, Pd, and Re were separated from the remaining solution using anion exchange chromatography, and then analyzed using the sector field ICP-MS Element 2 (Thermo) coupled with an Aridus II™ (CETAC) desolvating nebulizer. Standard NIST 3143 solutions were run with samples. Osmium concentrations and isotopic ratios were obtained using negative Thermal Ionization Mass Spectrometry. The samples were loaded with concentrated HBr onto Pt filaments with $Ba(OH)_2$ activator and analyzed as OsO_3^- using a Thermo Triton Plus thermal ionization spectrometer with a secondary electron multiplier in a peak hopping mode for samples with low Os concentrations. Internal precision for $^{187}Os/^{188}Os$ ratios was always equal to or better than ±0.3% ($2\sigma_m$).

2.3. X-Ray Diffraction (XRD)

Sample was homogenized in an ethanol suspension and analyzed with X-Ray powder diffraction using a Bruker D8 Advance instrument with CoKα radiation and a Lynx Eye XE detector. Diffractions were recorded in the range 4 - 80° of 2Θ angles with a step of 0.015° and qualitatively evaluated with the Diffrac.Eva software using the PDF 2 database. Semiquantitative phase analysis using the Rietveld method was performed with the Topas 5 software, with correction for preferential orientation at selected phases. Detection limits for crystalline phases were ca. 0.2 – 0.5 wt.%.

2.4. Scanning Electron Microscopy (SEM) and Microprobe Analyses (EMP)

Polished thin-sections were used. For imaging in back-scattered electrons (BSE) and secondary electrons (SE) as well as for microanalyses, prevalently the electron microscope and microprobe TESCAN Vega with energy-dispersive (EDS) analytical system and X-Max 50 detector was applied (Charles University, Prague). For details, also the microscope JEOL JSM-5510LV at the Czech Technical University and another TESCAN microscope at the University of Pardubice were used.

After finding the enstatite-rich meteorite fragment [13], a search for all Mg-rich objects was performed in both polished sections of MFa. This was achieved by automatic scanning of almost whole sections (the scanned areas were 900 and 864 mm^2, respectively) at the TESCAN demolab in Brno, Czech Republic. The samples were analyzed using a TESCAN Integrated Mineral analyzer (TIMA) based on an auto-emission scanning electron microscope (TESCAN MIRA) equipped with three ESSENCE EDS detectors. Beam current of 11 nA and high resolution analytical mode as described in [22] was used. Both the X-ray spectra and the BSE intensities were acquired in a regular grid defined by pixel spacing of 6 µm. Mounting epoxy was automatically excluded from the analysis using BSE threshold. 1000 X-ray counts were collected from each pixel. General classification scheme was used to specifically identify and locate all Ni, Cr and S bearing particles and Mg rich particles. Elemental maps for the target elements were also constructed.

For electron backscatter diffraction (EBSD), the TESCAN Mira3 GMU FEG-SEM with the EBSD system Symmetry (Oxford Instruments) at the Czech Geological Survey in Prague was used.

3. Results and Discussion

3.1. Bulk Composition of the Filling Fractions and Separated Glasses

 doi:10.20944/preprints202403.1621.v1

Results of chemical analyses are presented in Tables 1-3 (complete data are available in the supplementary Tables S1-3). TGA results are illustrated by supplementary Figure S1.

3.1.1. Major and Trace Element Wet Analyses

The relatively coarse gravel, i.e., pebbles washed from loam and containing no visible effects of melting, is rich in Ca, CO_2 and partly Mg, and poor in Al, Na and K; its mineral composition can be estimated to ca. 30-35 wt.% calcite, 20 wt.% dolomite, up to 30 wt.% quartz, and at most 20 wt.% silicates. In contrast, the finest fraction is formed mainly by silicates and quartz, and compared to gravel it is strongly depleted particularly in Ca. This can be explained by HT-decarbonization, which affected mainly fine-grained material and surface of pebbles, and formed burnt lime, i.e., CaO later transformed to $Ca(OH)_2$, which was partly dissolved and transported by groundwater, and partly formed a "mortar" and similar coatings on various pebbles (usually forming carbonate again); see also [15].

Content of elements whose concentration is typically high in surface glass on pebbles (K, Cu, Rb, Mn, Zn; see [15]) is higher in the fine fractions than in the pebbles (gravel), but there is no remarkable enrichment in these elements in comparison to most other elements (for K, this has also been confirmed by gamma-ray spectrometry [15]). The same holds for elements which could indicate contamination with iron metallurgy or iron/steel instruments (Fe, Mn, Cr, Ni), bronze (Cu, Sn), or other common metals (Pb, Zn).

3.1.2. TGA

Both samples of the fine filling fraction (bulk and NFa) show significant volatile loss starting with temperatures well below the range of decarbonization and dehydration of micas, excluding any intense heating of the most of the material to more than 100°C (see supplementary Figure S1). The total carbon content (3.5 wt.%) shows that organic matter cannot explain more than half of the ignition loss, which points to significant amount of thermally unaffected clay minerals in the filling. This shows that the fine fractions are rich in material which was prevalently brought only after the crater formation.

3.1.3. INAA

In Crater No. 4, MFa compared to NFa is enriched in Fe, Ti, Mn (but only slightly in Mg), Ta, Cr, Ni, Co, V, and rare earth elements (REE), especially the heavy ones (HREE). Concentrations of elements in SMF are mostly transitional between MFa and NFa, except for the highest content of light REE (LREE), Cs, Rb, Ba, and Zr in SMF. The bulk composition of the fine fraction is very close to that of NFa (relative difference is smaller than 3 % except for 6.5 % in the case of Cr). Most element contents determined by INAA in NFa are in good agreement with ICP-MS, except for significantly lower contents of Zr, Hf and partly HREE determined by ICP-MS, probably due to imperfect decomposition of zircon during the acidic dissolution. Regarding siderophile elements in MFa, the enrichment in Cr is most remarkable, while Ir was not detected and Au was detected above the detection limit (including blank) only in MFa1 (27 ppb) and in the SMF (7.5 ppb). Thus, significant influence of meteoritic contamination on the elements analyzed, even in MF, is uncertain.

Table 1. Bulk composition of gravel and fine sediment/soil fractions from Crater No. 4 (weighted mean from INAA represents the whole < 2mm fraction).

Wet analysis (wt.%)			**INAA** (oxides wt.%, halogens ppm)					
sample	**gravel**	**NFa**	**NFa1**	**NFa2**	**SMF**	**MFa1**	**MFa2**	**weighted mean**
SiO_2	39.92	60.29						
TiO_2	0.14	0.46	0.55	0.56	0.95	1.64	2.95	0.58
Al_2O_3	2.57	10.18	11.36	11.85	14.46	13.33	13.77	11.64
$Fe_2O_{3\,tot.}$	1.51	4.27	4.06	3.74	6.22	10.80	12.19	4.43
MnO	0.04	0.16	0.18	0.18	0.30	0.35	0.47	0.18

 doi:10.20944/preprints202403.1621.v1

MgO	5.40	2.49	2.01	2.42	2.84	2.60	3.00	2.23
CaO	24.25	4.10	3.19	3.83	2.91	2.94	3.13	3.50
Na_2O	0.46	0.99	1.04	1.03	0.93	0.85	0.92	1.04
K_2O	0.42	1.49	1.49	1.62	1.74	1.42	1.36	1.56
P_2O_5	0.05	0.16						
LOI	24.92	13.46	**Cl**	< d.l.	< d.l.	84.3	< d.l.	< d.l.
H_2O-	0.02	1.46	**Br**	7.61	7.10	8.70	7.75	6.67	7.4
Total	99.70	99.51	**I**	< d.l.	25.0	29.4	< d.l.	< d.l.
	ICP-MS (ppm)				**INAA** (ppm, Au ppb)			
Ba	54.6	340	334	339	553	296	457	338
Ce	11.3	57.0	64.7	62.6	108	94.1	95.4	64.2
Co	3.10	10.2	11.7	10.8	17.5	23.3	23.8	11.4
Cr	58.0	58.5	70.7	74.5	118	535	577	77.7
Cu	7.01	23.0						
Ni	9.09	32.5	28.0	28.8	43.0	68.0	62.5	28.8
Pb	6.76	23.1						
Rb	16.4	90.8	100	103	125	110	100	102
Sn	0.90	3.66						
Sr	209	108	103	98	118	104	105	100
Th	1.70	8.75	10.9	10.4	17.3	15.6	15.5	10.7
U	1.44	2.02	2.82	2.66	3.89	3.90	3.99	2.8
V	29.0	78.6	83.2	87.0	119.6	141.9	166.9	86.0
Zn			87	78	125	144	144	83.5
Zr	**6.46*	**21.5*	123	123	139	119	105	122.5
Au			< d.l.	< d.l.	7.5	27.2	< d.l.	

* values too low due to imperfect decomposition of zircon.

Table 2. Concentrations of selected elements in fractions of the fine-grained fillings of the Craters No. 4 and Crater No. 5 (data from LT-INAA only).

site	**Crater No. 4**					**Crater No. 5**			
grain size (mm)	**<0.063**	**0.063-0.1**		**0.1-0.25**		**< 2**			
sample	**fine fr.**	**MFb1**	**NFb1**	**MFb2**	**NFb2**	**MF**	**SMF**	**NF**	**weighted mean**
FeO t. (wt.%)	4.11	4.54	0.84	8.53	0.36	6.99	4.98	4.47	4.54
Na_2O	1.08	1.01	1.13	1.18	0.90	0.73	0.64	0.66	0.66
K_2O	1.51	1.48	0.97	1.25	1.01	1.10	1.23	1.21	1.21
Sc (ppm)	11.7	12.8	2.35	28.3	1.75	10.52	12.1	11.1	11.1
Cr	79.3	216	24.36	521.5	8.81	102.1	81.4	69.5	70.52
Co	11.7	12.64	2.2	14.25	0.686	19.7	16.3	14.6	14.72
Ni	38.0*	34.3	< d.l.	24.7*	< d.l.	43.5*	43.1	47.1*	46.94
Zn	91.9	109.4	26.9	120.5	10.73	115.25	119.9	109.7	110.0
As	11.1	12.27	3.6	11.8	1.44	24.87	23.73	21.95	22.05
Rb	99.7	96.8	41.8	76.1	40.3	74.3	94.9	90.4	90.1
Sr	96.5	135.1	90.8	130*	25.9**	88.1*	< d.l.	< d.l.	
Zr	137.4	171.3	282.6	157.5*	126.6	97.5*	77.4*	95.8*	95.5
Sb	1.36	1.42	0.47	1.9	0.437	3.88	4.4	4.36	4.35
Cs	4.58	4.45	1.31	3.35	1.11	4.4	5.9	5.57	5.55
Ba	383	1756	3604	503	182	221	252	244	243
La	42.20	46.27	7.16	112.6	4.975	31.0	38.0	34.3	34.3
Ce	70.30	79.51	11.96	186.5	8.66	53.7	63.3	56.6	56.7

 doi:10.20944/preprints202403.1621.v1

Yb	3.15	3.19	0.90	5.92	0.489	2.75	2.61	2.46	2.47
Hf	7.66	7.88	12.45	6.76	5.685	4.14	4.22	4.38	4.37
Ta	0.916	1.27	0.335	2.05	0.315	0.97	0.838	0.813	0.82
W	1.39**	26.59	16.73	2.18**	< d.l.	1.30**	1.86*	1.58**	1.63
Th	10.95	12.88	2.50	30.19	2.25	7.93	9.35	8.66	8.65
U	< d.l.	3.48*	1.61	2.65	< d.l.	2.64	2.48	2.0	2.03
Au (ppb)	< d.l.	< d.l.	< d.l.	< d.l.	58.7	< d.l.	< d.l.	< d.l.	

* relative uncertainty >10%, ** relative uncertainty > 20%.

Table 3. Concentrations of selected elements in molten rock and glasses (manually separated) from Crater No. 4, and glass coatings of an orthogneiss pebble from the Kaltenbach structure and of an amphibolite pebble (Ko-085) from a ruin of limekiln at Frechensee, Seeshaupt (data from LT-INAA only).

sample	**4/2/1a1 (Crater No. 4)**						**123 (Kalt.)**	**Ko-085**
position	surface	interior	surface	injection	interior	interior	surface	surface
color	black	colorless	light green-yellow	black	light, quartz-rich	white	green	dark green
FeO t. (wt.%)	6.19	1.13	0.60	6.63	0.63	0.32	1.29	4.10
Na_2O	3.56	2.82	6.10	4.26	6.33	4.56	6.22	4.84
K_2O	5.02	4.19	0.96 *	3.38	0.78 *	2.29	8.47	16.66
Sc (ppm)	16.2	2.01	1.97	14.9	2.15	1.37	5.18	6.13
Cr	46.2	6.79	4.48	47.2	0.88 **	5.31	1.78 *	29.4
Co	10.3	2.16	1.13	10.5	0.51	0.55	1.585	39.0
Ni	< d.l.	< d.l.	< d.l.	29.1 **	< d.l.	< d.l.	< d.l.	98.9
Zn	107.1	20.35	< d.l.	89.4	< d.l.	< d.l.	35.8	153.65
As	< d.l.	6.0	< d.l.	< d.l.	< d.l.	< d.l.	< d.l.	2.92
Rb	209.7	102.8	45.4	168	18.5	46	535.6	400.2
Sr	67.8 *	40.2 *	112.7	< d.l.	162.1	59	< d.l.	97.6
Zr	184.1	18.0 **	44.1	140	44.4 *	37.9	< d.l.	38.1**
Sb	0.66	0.24	< d.l.	0.55	< d.l.	< d.l.	< d.l.	0.317
Cs	5.07	1.25	1.18	4.82	0.24	0.90	6.6	6.78
Ba	590	622	118	498	145	141	143	228
La	32.94	7.2	6.26	31	5.36	5.9	3.35	17.06
Ce	59.1	18.1	12.55	72	12.3	11.1	6.63	32.2
Yb	4.83	0.47	2.205	4.27	2.98	1.6	0.837	1.31
Hf	11.7	1.145	1.95	8.9	1.30	1.28	0.862	2.84
Ta	3.44	0.245	2.29	3.9	2.74	2.27	8.64	0.464
W	< d.l.	< d.l.	< d.l.	< d.l.	< d.l.	< d.l.	< d.l.	< d.l.
Th	32.9	4.67	10.55	22.9	12.61	6.85	4.8	5.87
U	4.6 *	< d.l.	6.22	< d.l.	7.45	4.69	< d.l.	< d.l.
Au (ppb)	< d.l.	< d.l.	75.8 *	< d.l.	< d.l.	< d.l.	< d.l.	< d.l.

* relative uncertainty >10%, ** relative uncertainty > 20%.

The electromagnetic separation after sieving led to greater contrasts between MF and NF, with NFb poor in Fe, Cr, and Co. Especially the NFb1 and MFb1 are rich in Ba (0.36 and 0.176 wt.%, respectively). MFb also concentrates monazite (in contrast to zircon), with the peak value for the sum of LREE in MFb2 (401 ppm, with 30.2 ppm Th). The most enriched element in MFb relatively to NFb is again Cr. Both MFb1 and NFb1 have relatively high content of W (26.6 and 16.7 ppm, respectively),

 doi:10.20944/preprints202403.1621.v1

which is however low in all other samples. Gold was only detected in NFb2 (58.7 ppb), and Ir was not detected. The fraction finer than 0.063 mm has slightly higher Ni content but much lower Cr content than MFb.

Similarly, the chemical composition of glass coatings on pebbles lacks an evidence for meteoritic contamination. Nickel concentration is even smaller than in the glass coating from limekiln where there is no reason for such a contamination (although it could be influenced by the basic substrate rock). Out of HSE, only Au and Ir were measured. Gold was detected only in one sample (nevertheless with a relatively high concentration), and Ir was not detected above detection limits of 1.3–3.6 ppb. If we assume a maximum Ir concentration in our samples to be 2 ppb, the contamination with chondritic material which contains ca. 0.5 ppm Ir [23] should not exceed 0.4 wt. % (not taking potential chemical fractionation into account).

In the filling of Crater No. 5, the chemical differences between the magnetic and non-magnetic fractions are small. Also the proportion of MF (2.5 %) and SMF (1.7 %) is higher than in Crater No. 4. Content of most metals in NF (and consequently in the whole filling as well) is higher in Crater No. 5 than in Crater No. 4. The greatest difference between both craters is observed for Sb, i.e., a metalloid. The chemical similarity of MF and NF in Crater No. 5 suggests that the metals and metalloids are rather concentrated in or sorbed on organic matter, clay minerals, and non-magnetic Fe-hydroxides. Common concentrating these elements in fine-grained recent alluvial sediments, usually enhanced by anthropogenic pollution, seems to be a more likely explanation than a significant meteoritic contamination.

3.1.4. HSE and Os Isotope Ratios

The enrichment of MF in PGE compared to NF (Table 4) is less contrasting than the enrichment in Cr. The most relatively enriched HSE in MF are Ir and Ru, less enriched Os and Pt, while the differences in Pd and Re concentrations are insignificant. According to PGE, the magnetic fraction cannot contain more than 10^{-4} of chondritic or 10^{-3} of achondritic material, which is an upper limit due to the PGE budget from terrestrial rocks.

Table 4. Concentrations of HSE (ppb), and Os isotope ratios in the bulk fine filling fraction (< 2mm) and in the magnetic fraction (MFa) separated from it.

fraction	Re	Os	Ir	Ru	Pt	Pd	$^{187}Os/^{188}Os$
Bulk	0.214	0.028	0.018	0.021	0.31	0.20	2.24
Magnetic	0.201	0.059	0.095	0.079	0.49	0.19	1.113

Vast majority of PGE in ultrabasic rocks is allocated to sulfides (96 % according to [24]). As shown in 3.2., no sulfides were observed in the detrital rocks in the crater filling. They were oxidized during weathering and transport, and it is questionable to what extent PGE could be retained. The PGE may be contained in submicroscopic nuggets or Fe oxides formed as sulfide alteration products. These particles, unless they were lost during separation, are likely associated (agglomerated) with various minerals or included in serpentine, making their magnetic separation little efficient.

Magnetic separation, however, concentrated PGE contained in chromite. The partitioning of PGE into chromite is strongly dependent on oxygen fugacity, being one to three orders of magnitude higher in spinels enriched in ferric iron [25]. Our EMP data do not support significant presence of Fe^{III} in chromite. Osmium concentration in chromite of ophiolites is usually in the order of tens of ppb [26]. According to Cr concentration, chromite makes up to 0.14 wt.% of MF. Therefore, if only chromite accounts for the excess Os in MF compared to NF, it should contain ca. 25 ppb Os, which is acceptable. The most compatible PGE in chromite is probably Ru [25] which is also strongly enriched in MF relatively to NF.

In NF, crustal rocks dominate the PGE budget, as evidenced by the Os isotope ratio (compared to the $^{187}Os/^{188}Os$ ratios < 0.130 in chondrites [23]).

3.2. Mineralogy and Microchemistry of Crater No. 4 Filling

 doi:10.20944/preprints202403.1621.v1

3.2.1. Overview and Comparison of Magnetic and Non-Magnetic Fractions

Semiquantitative mineral composition of MFa is provided by XRD (Table 5). Due to inclusions, intergrowths, etc., and imperfect separation, non-magnetic minerals prevail. Fe oxides in both MF and NF are commonly mixed or intergrown with non-magnetic minerals (quartz, feldspars, clay minerals, zircon, calcite, dolomite) and in some cases they may represent limonite dehydrated and transformed to magnetic oxides by heating. It is unclear whether some agglomerates of grains of various minerals could be chemically cemented or thermally sintered. Contrary to pebbles, fragments of melt glass are little abundant. Thanks to the microscopic to submicroscopic magnetite (see also [15]), glass is more common in MF than in NF.

Table 5. Mineral composition of the magnetic fraction (MFa) as determined by XRD.

Mineral	**dolomite**	**chlorite**	**quartz**	**micas**	**plagioclase**	**K-feldspar**
wt. %	1	10	56	10	11.5	2.5

Mineral	**hematite**	**ilmenite**	**amphibole**	**magnetite**	**goethite**
wt. %	1.5	1	4	2	uncertain

The magnetic or potentially magnetic minerals identified in MFa and MFb1 are magnetite, ilmenite, garnet (almandine or spessartine), rutile (possibly also other TiO_2 phases), chromite, magnesiochromite, serpentine, chlorite, biotite, rare diopside, sphene, zoisite, monazite, siderite, ankerite, amphibole, apatite, and xenotime. Iron oxide particles formed by oxidation of spheroid pyrite framboids are common. An object exceptionally rich in framboidal oxides was identified as a fragment of marine foraminifera shell (*Bulimina*) which had to be transported from Alps. Nevertheless, local origin (possibly from a framboid) is probable in case of a nearly perfect but porous spherule (30 μm in diameter) formed by siderite and ankerite.

In NF, the amount of carbonates, though higher than in MF, is relatively small, consistent with the bulk chemical composition. Abundant acicular microfossils are visible in stereomicroscope, probably representing silica spicules from sponges. In contrast, carbonate microfossils have not been identified. Corrosion layers rich in quartz and silicates were observed even on small carbonate grains. Calcite, dolomite (including replacement of calcite) and siderite (as inclusions in calcite) were identified with EMP in NFb1. The dominant mineral is quartz; hollow rounded grains and crystals could represent hydrothermal quartz. Nevertheless, the presence of non-crystalline silica and even lechatelierite is possible (in both NF and MF). Feldspars, white mica, and clay minerals are common. Out of accessory minerals, NF is characterized by abundant barite (see also Table 2 for the high Ba content in NFb1) and zircon.

In contrast to impact-affected pebbles where especially quartz and zircon are commonly strongly fractured and even penetrated by melt (see [15]), these minerals in both MF and NF do not show such features. It seems that isolated mineral grains responded to the compression by formation of compact aggregates rather than fracturing, and that the fracturing cannot be explained solely by temperature changes.

3.2.2. Main Findings in the Magnetic Fraction

This section deals mainly with the closely investigated MFa unless stated otherwise.

3.2.2.1. Well-Preserved Meteorite Fragment

The best preserved meteorite fragment (Figure 2) is almost 90 μm long in the section. Its shape as well as lack of supergene alteration excludes any significant water or on-ground transport. Ablation surface is not observed. The dominant mineral is enstatite ($Fs_{2\text{-}3}Wo_1$, with significant admixtures of Cr and Al; see Table 6). For simplicity, we use the term 'enstatite' (s.l.) for all $MgSiO_3$ pyroxene polymorphs. There is a minor amount of forsterite ($Fa_{4\text{-}5}$) and highly basic plagioclase (An_{90}).

 doi:10.20944/preprints202403.1621.v1

Metallic iron with Ni (Table 6) is the first evidence of meteoritic origin. Nickel content in the largest iron metal grain is ca. 5.5 wt.%. In small metal grains, Ni content measured varies from 4 to 11 wt.%; these analyses are influenced with surrounding enstatite and/or other phases which however should not significantly alter the Fe/Ni mass ratios, ranging from 7.4 to 16.1. Therefore, the metal corresponds to α-(Fe,Ni) (kamacite) which was also confirmed by EBSD. Nickel-rich Fe sulfide is common. The (Fe+Ni)/S molar ratio of the sulfide ranges from 0.88 to 0.94, corresponding to pyrrhotite, and the Ni/(Fe+Ni) molar ratios form two distinct groups (0.066–0.078 and 0.23–0.26). According to EBSD, however, the structure of the sulfide (especially in the largest grain) mostly corresponds to troilite rather than pyrrhotite. In addition, the crystallographic orientation of (minor) pyrrhotite in this grain is rather chaotically distributed. These results indicate an imperfect alteration of troilite to pyrrhotite.

The texture resembles a cumulate with small amount of a relatively Mg-poor finely crystallized intercumulus melt which contains plagioclase (slightly less basic than larger crystals) and perhaps diopside (Figure 2A on the left, 2d; note that these grains are too small for quantitative EMP analyses), in places with a thin reaction rim in adjacent enstatite. This suggests a magmatic differentiation, characteristic for achondrites.

An unspecified silica phase was found which shows no diffraction in EBSD. A Ca-rich phosphate associated with sulfide is most likely merrillite $Ca_9MgNa(PO_4)_7$, a mineral common in meteorites but very scarce otherwise [27]. However, measurement not influenced by surrounding phases was not possible.

EBSD shows that the Ca-poor pyroxene is prevalently low clinoenstatite ($P2_1/c$) twinned on (100), with apparent width of the twin lamellae from 1 to 3 μm (they are also visible in cross-polarized light; see Figure 2B). Low clinoenstatite is typical (though not diagnostic) for meteorites ([28] and references therein; [27]). A crystallographically homogeneous band (ca. 5×20 μm) of orthoenstatite (Pbca), nearly parallel to the twin-lamellae of adjacent clinoenstatite, was also identified by EBSD on the rim of meteorite's cross-section (right bottom in Figure 2A-C). Only weak fracturing is observed in enstatite but abundant short cracks perpendicular to the twin lamellae are observed (Figure 2A,B,E bottom). They probably represent contraction cracks formed by phase transition from protoenstatite at cooling (see [29]). The small portion of orthoenstatite suggests a fast cooling in the orthoenstatite stability interval (ca. 600-1000 °C at low pressure; [28]) or slow cooling at lower temperatures facilitating crystallization of clinoenstatite.

No unequivocal evidence of shock has been observed (compare [30]), although some deformation of the twin lamellae is visible, and submicron-thick, probably Fe-rich veinlets parallel to the twin lamellae occur in enstatite (Figure 2B,E in the middle).

EBSD confirmed monocrystalline character of forsterite, plagioclase, and kamacite. Most metallic and sulfidic grains are partly to completely rimmed by a Ca-rich reaction phase (Figure 2E).

 doi:10.20944/preprints202403.1621.v1

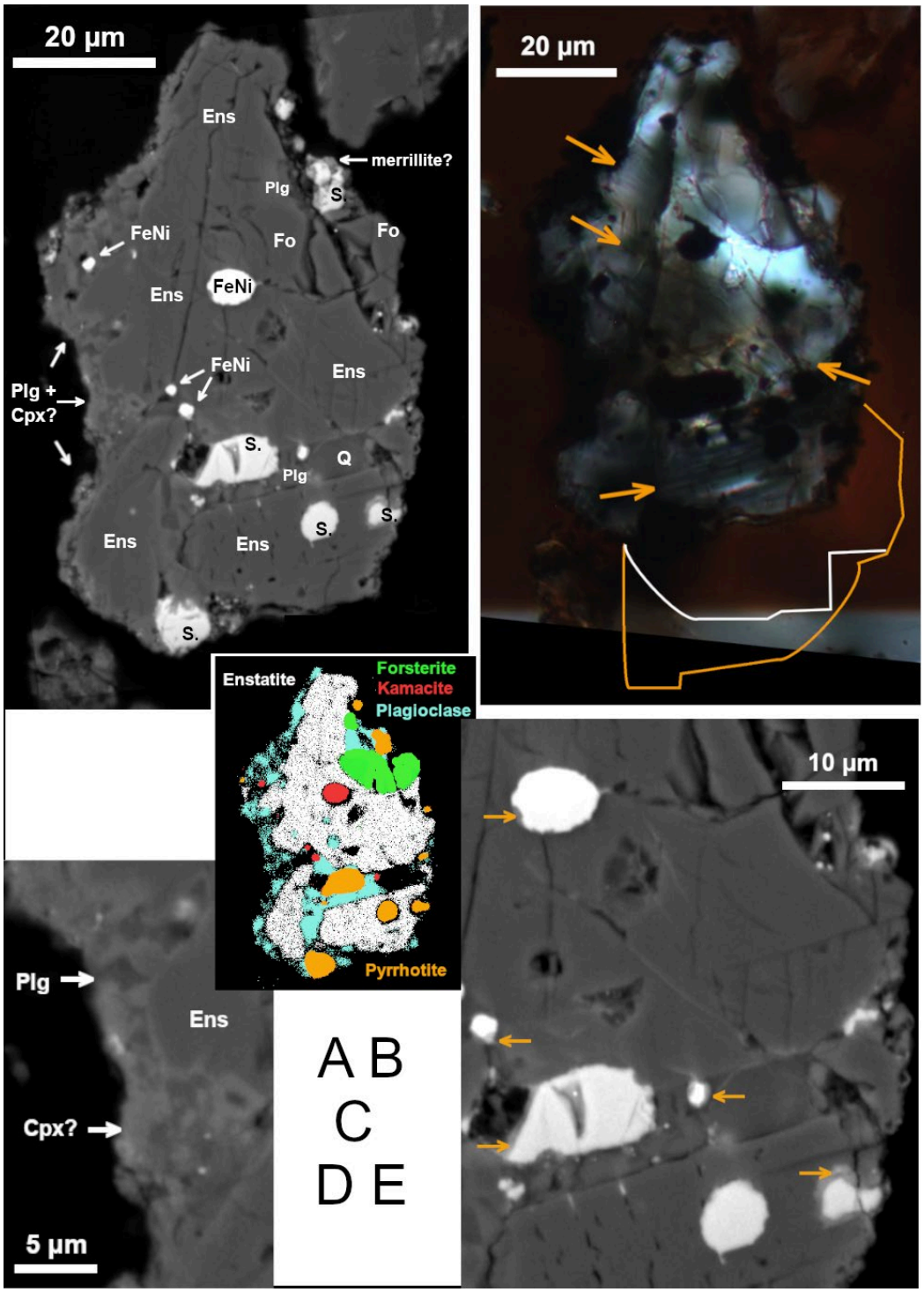

Figure 2. Meteorite fragment. (**A**) BSE image. Mineral labels: Ens – enstatite (prevalently clinoenstatite), S. – Fe-Ni sulfide, FeNi – metallic iron (kamacite), Fo – forsterite, Plg – basic plagioclase, Q – silica, Cpx – clinopyroxene. (**B**) Image in transmitted light (crossed polars, slightly askew). Arrows point to the clinoenstatite twin lamellae. The orange and white lines delimit the maximal- and minimal, respectively, additional subsurface extent of the object. (**C**) Map of the main mineral phases (based on spot analyses and element maps from EMP). (**D**) A detail of the probable intercumulus melt, containing plagioclase (relatively dark) and perhaps clinopyroxene (BSE). (**E**) A detail (in BSE) showing reaction phases at the rim of sulfide and metal grains (darker than sulfide/metal but brighter than the surrounding silicates; see arrows). Note the contraction cracks (bottom), fractures (middle right), and thin brighter veinlets (middle) in enstatite.

 doi:10.20944/preprints202403.1621.v1

Table 6. EMP analyses of enstatite, sulfides, and metallic iron in meteorite (Figure 2).

		SiO_2	TiO_2	Al_2O_3	Cr_2O_3	FeO	NiO	MgO	MnO	CaO	Total
Enstatite	oxide wt. %	57.55		0.57	0.98	1.79	0.22	37.44		0.63	99.17
		56.61	0.17	0.53	0.80	1.39	0.05	36.89		0.67	97.11
		56.74	0.19	0.9	0.81	1.12	0.23	37.07	0.23	0.77	98.07
	cations / 3O	Si	Ti	Al	Cr	Fe	Ni	Mg	Mn	Ca	Total
		0.985		0.012	0.013	0.026	0.003	0.954		0.012	2.003
		0.987	0.002	0.011	0.011	0.02	0.0005	0.955		0.013	1.999
		0.978	0.003	0.018	0.011	0.016	0.003	0.957	0.004	0.014	2.004

wt. %	**O**	**Mg**	**Al**	**Si**	**S**	**Ca**	**Ti**	**V**	**Cr**	**Mn**	**Fe**	**Co**	**Ni**	**Total**
Sulfide	0.62	0.16	0.08	0.54	37.31				0.14	0.28	54.99	0.66	3.88	98.66
		0.05	0.05	0.09	38.57	0.08	0.09		0.06		44.2		16.34	99.53
				0.19	38.37	0.06		0.01	0.08		43.6		16.47	98.78
				0.11	37.51	0.08					43.98		15.97	97.65
		0.2	0.04	0.27	37.69						54.99		4.65	97.84
Metal				0.11					0.09		89.03		5.21	94.44
				0.07				0.05	0.1		88.29	0.97	5.48	94.96
	1.44	0.18		0.45	1.01	0.09	0.03		0.09		88.57		6.36	98.22

3.2.2.2. Remelted Meteorite Fragments

The most Ni-rich object found by the scanning is a slightly rounded Mg-rich silicate glass with a cavity which is divided into two major parts in the section. The Ni-rich minerals form mainly the cavity interior and walls (Figures 3, 4). The association can be interpreted as a result of reactions of silicate melt with metallic melt and/or molten sulfides from which sulfur largely volatilized during the impact (see [31]), and the remaining S-rich minerals may have been removed by weathering. Enrichment in Ni could be explained by partial oxidation. Experiments with iron meteoritic projectiles [32] and observations of natural melts in impact craters [33] showed that the metallic phase affected by melting is relatively depleted in Fe due to its preferential oxidation [34], and, consequently, enriched in Ni, while Fe partitions more than Ni into the silicate melt [32,35]. Thus the Ni-oxide (Figure 4) may represent a later oxidized nickel metal.

The remaining Mg-rich meteorite-derived objects are formed by highly porous glass chemically similar to enstatite or forsterite with only minor amount of tiny Fe-oxide grains. The glass usually contains Fe, Ca and Al,, and minor Ni admixture is commonly detected (up to 0.83 % in spots influenced by Fe-rich inclusions). The bulk composition of the Mg-rich glass particles is consistent with that expected for the enstatite-rich meteorite. Only K content in glass (up to 2 wt.%) is relatively high. In finely porous domains also Cl is commonly detected which, however, may represent the epoxy resin. In several, rather small cavities tiny crystals formed including olivine (Figure 5 A,B), and locally diopside and possibly Ca-Mg amphibole crystallized in cavities or directly from glass. Some Mg-rich glasses have a more porous rim, enriched in Ca (Figure 5 C,D). A probable submicron-sized relict of unoxidized kamacite was found.

The Mg-rich glasses never form sharp-edged clasts; instead, their forms resemble somewhat deformed droplets. The enrichment in K may be related to their porosity and could be explained by influence of a K-rich fluid during crater formation, similar to K-rich glass coatings on the pebbles. The Ca-rich rims very likely reflect reactions with post-impact Ca-rich solutions influenced by dissolved lime (see [15]).

 doi:10.20944/preprints202403.1621.v1

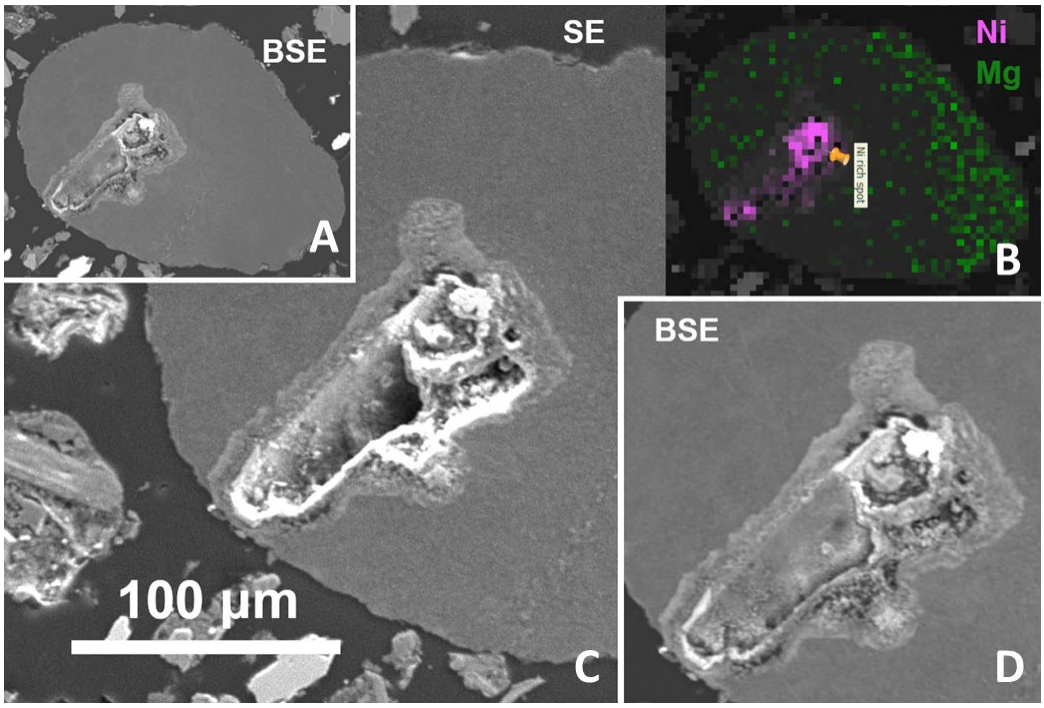

Figure 3. A probable remelted meteorite fragment: Ni and Fe-rich minerals in Mg-rich glass. (**A**) Overview in BSE. (**B**) Highest concentrations of Ni and Mg indicated in colors (from scanning of the whole section). (**C**), (**D**) Details in SE and BSE, respectively (note that the SE and BSE signals are not pure but somewhat mixed).

3.2.2.3. Terrestrial Ultrabasic and Basic Rocks, and Derived Melts

In serpentinite clasts, serpentine usually forms aggregates of lath-shaped crystals but it can also form continuous masses with some fracturing (Figure 6A). It is usually associated with magnetite. Locally, serpentine is associated with diopside which could be preserved from the original peridotite (lherzolite or wehrlite). Presence of olivine relics in some serpentinite clasts is uncertain.

Chromite has usually a strong predominance of Fe over Mg. An inclusion of olivine (Fa_{17}) has been observed in chromite. Magnesiochromite was also found, including a relatively large grain (more than 100 µm in length, rimmed by talc which formed by alteration of Mg-rich silicates). Also interesting is the presence of Zn-bearing chromite, locally associated with unspecified Cr-rich silicate. Meteoritic origin of a minor portion of chromite cannot be excluded. Note that chromite is important to identify fossil meteorites of which other minerals decomposed, e.g., in meteorite-rich Ordovician limestones in Fennoscandia where also Zn-rich chromite was found [36].

A rather fine-grained rock, probably tectonically affected gabbro with a weak oxidizing alteration, consists mainly of diopside, plagioclase (An_{56-64}), and magnetite, and has no obvious manifestation of melting (Figure 7A). Amphibolite, relatively fine-grained and comparable to a control thermally unaffected amphibolite pebble, consists of hornblende, plagioclase (An_{14}), and rutile (Figure 7C). Another probable basic rock (greenschist?) contains actinolite (in places chloritized) and albite (An < 10%). Also sphene occurs, sometimes associated with ilmenite. An example of molten basic rock is shown in Figure 7B. It is formed by porous glass with abundant euhedral to subhedral small crystals of diopside.

No sulfide preserved has been found in the filling except for the Ni-rich pyrrhotite in meteorite (note that also scanning of two whole sections of MF for sulfur was used).

 doi:10.20944/preprints202403.1621.v1

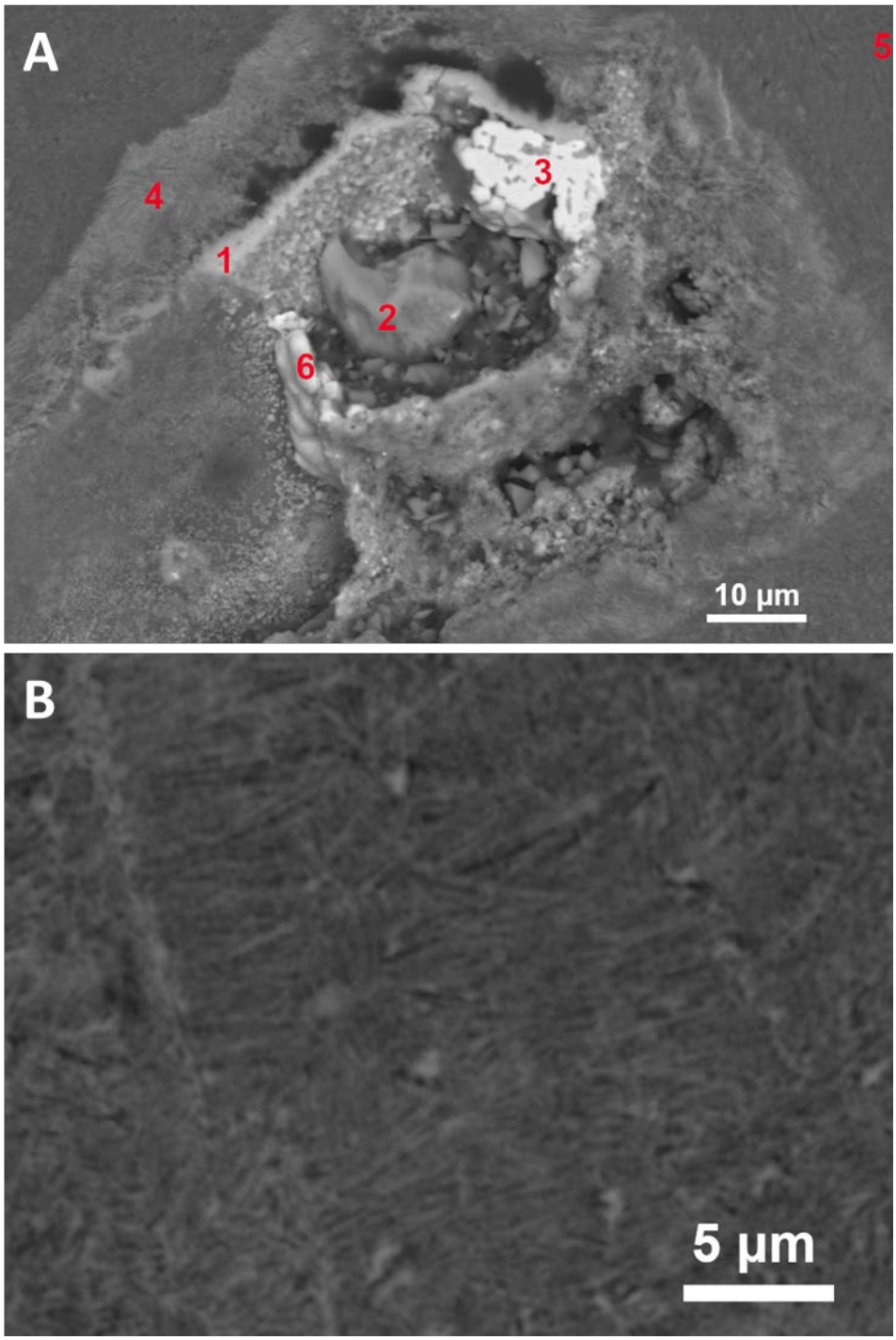

Figure 4. (**A**) Detail of the Ni-rich minerals (Figure 3). Phases analyzed: 1. silicate of Fe, Ni and Mg (olivine?), 2. silicate of Ni, Fe, Al, and Ca (possibly mixed with oxide phase), 3. Ni oxide (possibly incompletely oxidized metal; Fe ≤ 20 wt.%) with a darker interstitial Mg silicate, 4. Fe-Mg silicate (olivine?) containing Al (in other phase?) and Mn, Ca, and Ni, 5. silicate glass (see analysis in Table 7) containing Mg, Fe, and Al (with minor Mn), 6. oxidic compound of Ni (~50 wt.%) and Fe. (**B**) Detail of the silicate matrix with abundant small pores further from the Ni-rich minerals; two phases can be distinguished: silicate glass (dark) and probably silicate glass with submicroscopic Fe and Mn oxides (bright) which may have formed as a weathering product.

Table 7. EMP analyses of Mg-rich glasses (cations normalized to 6 O; total Fe as Fe^{2+}).

classification	Na	Mg	Al	Si	K	Ca	Mn	Fe	Ni	comment
weathered?	0.98	0.27	1.97		0.06	0.18	0.42	0.02		Fig. 4A (an. 5)

 doi:10.20944/preprints202403.1621.v1

weathered?	1.02	0.25	1.94	0.01	0.06	0.15	0.50	0.02	Fig. 3
fresh	1.58	0.09	1.98	0.06	0.11		0.15	0.02	Fig. 5B (an. 4)
fresh	1.64	0.08	1.98	0.13	0.05		0.16		
fresh	1.72	0.08	1.94	0.08	0.09	0.01	0.15		
fresh	1.74		1.98		0.05		0.25		
fresh	2.28		1.64		0.08		0.38		
fresh	0.11	2.31		1.66	0.04	0.07	0.23		Fig. 5C
altered	0.01	0.71	0.16	1.85	0.02	0.78	0.52		Fig. 5C; traces Ti, S
fresh	0.09	2.33		1.60	0.05	0.06	0.35		Fig. 5D
altered		0.87	0.16	1.84	0.01	0.88	0.33	0.01	Fig. 5D

Impact melting of the basic rocks observed can explain the secondary projectiles and injections of basic melts into quartz-dominated pebbles, as documented in [15] (see also [14]). It was suggested [8,37] that some of these basic melts may represent an achondritic projectile. While the achondritic composition of the projectile is probable, these melts are relatively rich in Ca and Al and poor in Mg as compared to the meteorite. Therefore, remelted basic or intermediate regional rocks tentatively seem to dominate the dark melt injections and surface contaminations, although participation of diopside-plagioclase domains of the meteorite (which could be preferentially melted) cannot be excluded.

On the other hand, it is improbable that melting of ultrabasic rocks with abundant magnetite and/or chromite, or of Ca-rich basic rocks, could explain the formation of Mg-rich but Fe, Cr, and Ca-poor glasses. Note that enstatite partially melts only above 1500 °C producing forsterite, which melts at temperature up to 1890 °C [38]. Serpentine dehydrates to form forsterite at low temperature (<500 °C; [38]). The very high melting temperature of forsterite, which is also the final solid phase after heating of various Mg-rich silicates, is another line of evidence, making any speculations about anthropogenic melting highly problematic. And, of course, the meteorite fragment with primary minerals preserved (including kamacite, and probably merrillite and troilite) cannot be compared to any regional rock.

3.2.2.4. Fragments of Quartz-Rich Rocks Affected by Melting

Many silicate pebbles in the crater were affected by melting of biotite, in places influenced by feldspars, forming typically glass with fine crystals, especially of magnetite, and locally with high porosity (see also [15]). The intergrowth of such glasses with the original quartz (Figure 8) proves unequivocally their origin from local rocks.

3.2.2.5. Hollow Spheroid Particles

Two smooth Fe oxide spherules were found. The first one (Figure 9A) contains admixtures of Si, Al, and Mg, but the other, morphologically almost perfect (Figure 9B), is chemically homogeneous and almost free of admixtures. Another Fe oxide particle with radial structure (Figure 9C) contains admixtures of Si, Ca, P, Mg, and Al. A strong affinity of P to ferric iron in sediments and soils suggests that the radial particle formed from limonite. Hollow Fe oxide spherules of similar, Ni-poor composition are abundant, in addition to distal sites (see 3.6), in a probable impact crater of the Bajada del Diablo crater field, Argentina [39].

 doi:10.20944/preprints202403.1621.v1

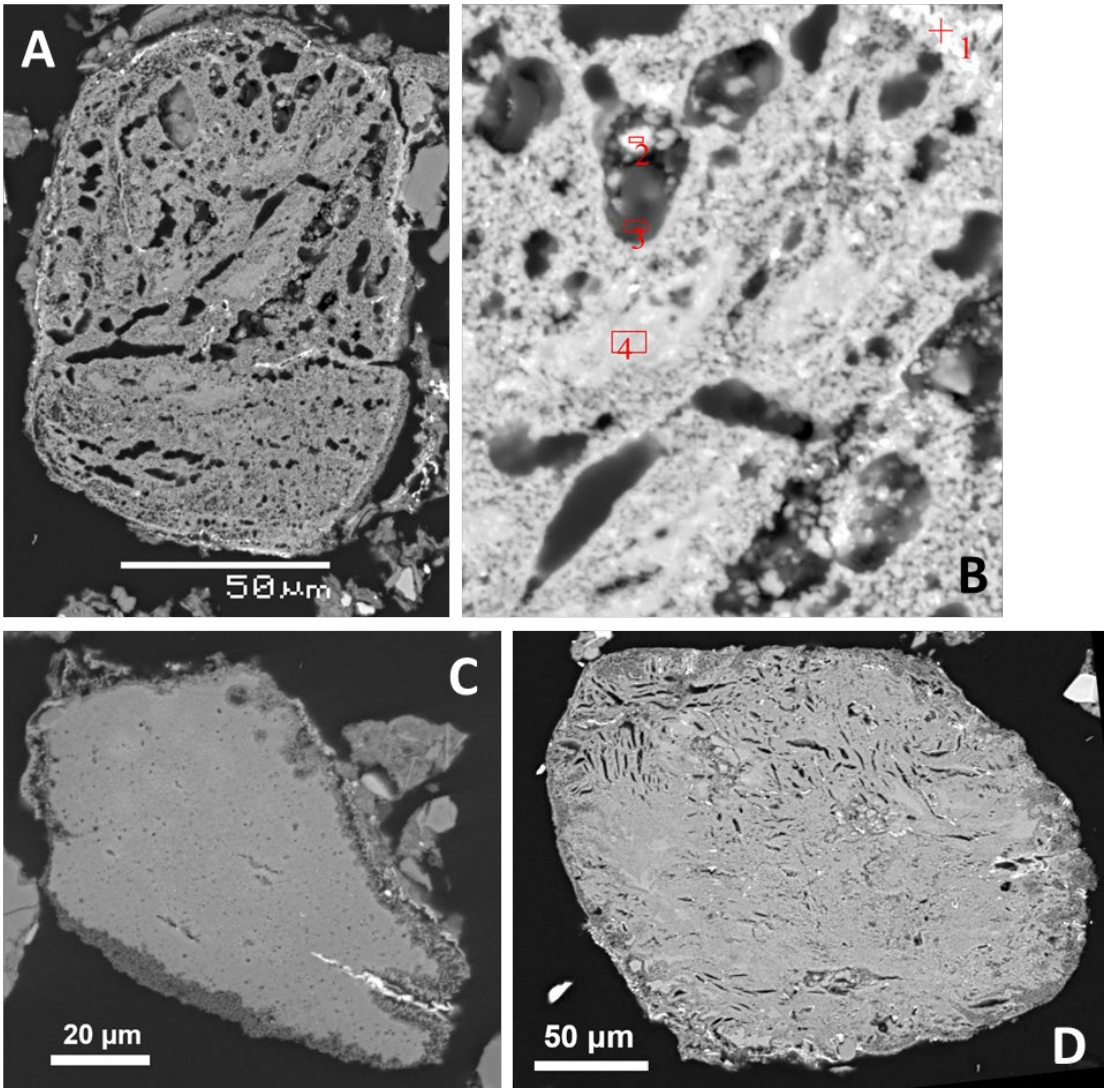

Figure 5. Other Mg-rich glasses (see also Table 7). (**A**) Highly porous object chemically close to enstatite. (**B**) Detail with spots analyzed. (**C**) Glass with altered, Ca-enriched rim with fine pores. (**D**) Glass locally with porous, Ca-enriched rims; EBSD showed scarce relics of forsterite structure in the Mg-rich glass.

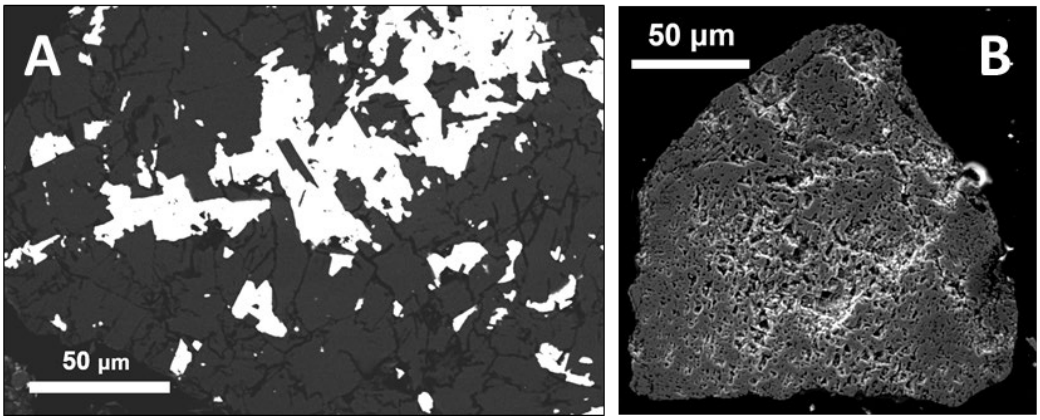

Figure 6. (**A**) Serpentinite fragment: dark serpentine and bright magnetite (BSE image). (**B**) Chromite (an unusually porous grain), SE image.

 doi:10.20944/preprints202403.1621.v1

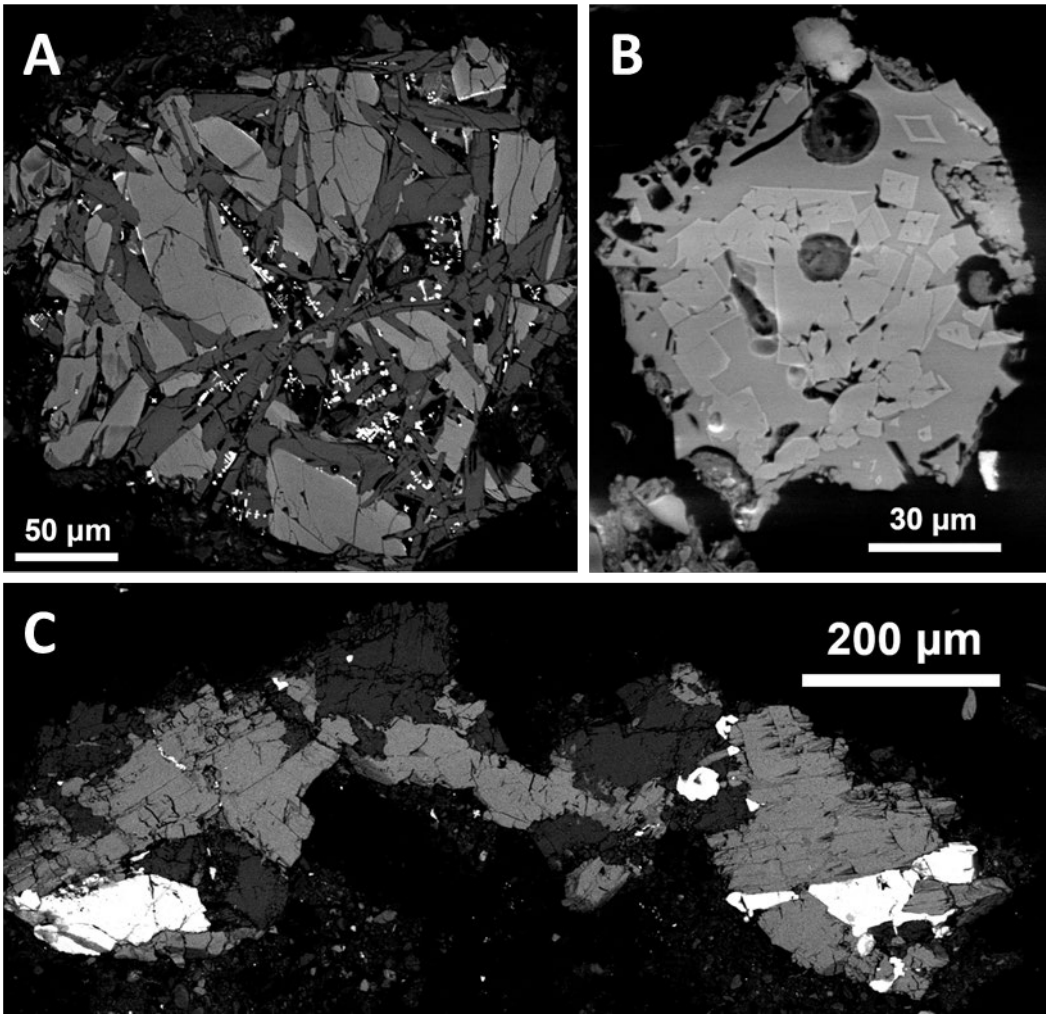

Figure 7. (**A**) Probably unmelted basic rock fragment formed by brecciated diopside (light grey) with younger plagioclase (grey) and magnetite (white); magnetite and plagioclase are possibly locally associated with secondary silicates (dark; formation of glass cannot be excluded). (**B**) Fragment of in-situ melted basic rock (in MFb) – small diopside crystals in glass with spherical pores and conchoidal fracture. (**C**) Amphibolite formed by an amphibole similar to hornblende (light grey, most cleaved), plagioclase (dark grey) and rutile (white).

The Mn oxide hollow spherule (Figure 9D) formed from Mn-rich weathering products. It contains a small particle of Ce oxide which reflects the affinity of tetravalent Ce to both Fe and Mn oxides and hydroxides [40]. Only one such spherule has been found but detailed search of the whole samples for such small objects would be very time-consuming (even with automatic scanning). During heating, the most common Mn oxide mineral – pyrolusite (MnO_2) – is reduced to Mn_2O_3 and then to Mn_3O_4 at relatively low temperatures; Mn_3O_4 melts at 1705 °C [41], and similar patterns can be expected for oxides formed by thermal dehydration of Mn hydroxides.

Hollow spheroid SiO_2 particles with complicated interior were observed in both magnetic (Figure 9E) and non-magnetic fractions. They may represent clasts of hydrothermal quartz.

 doi:10.20944/preprints202403.1621.v1

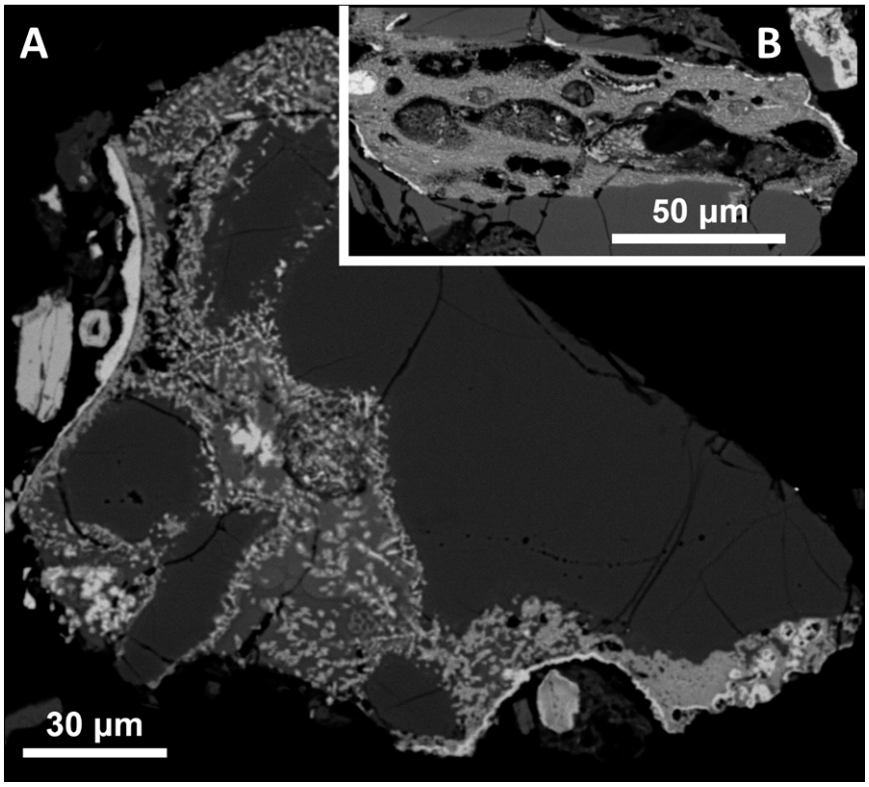

Figure 8. (**A**) Quartz with silicate glass from which mainly fine magnetite crystallized. (**B**) Expanded biotite-derived melt glass in another quartz.

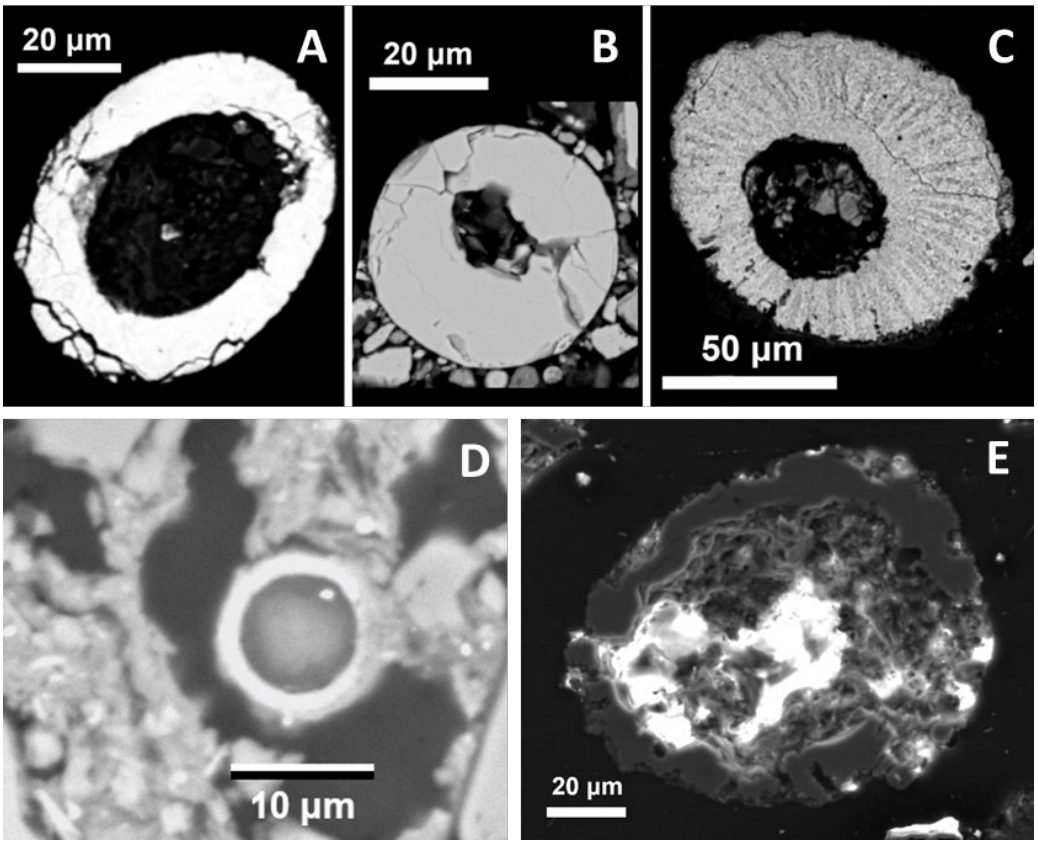

 doi:10.20944/preprints202403.1621.v1

Figure 9. Hollow spheroid particles (A-D: BSE images, E: SE image). (**A**), (**B**) Fe oxide with a smooth surface. (**C**) Fe oxide with radiating surface. (**D**) Mn oxide with small bright inclusion of cerium oxide (in MFb1). (**D**) Silica; note the complicated inner surface.

3.2.2.6. Other Objects of Unclear Origin

More conspicuous objects were found: an example is an aggregate of quartz with minor silicates, Fe oxide and occasionally rutile (Figure 10). One possibility how to explain such mineral compositions, which are unlikely in a single rock fragment, is a compaction by the pressure wave. A possible analogue is the shock-lithified sandstone documented in the Wabar craters [42]. In experiments with dry sandstone, shock pressure not greater than 2.5 GPa was sufficient for complete pore space collapse [43].

An aggregate of Fe oxide which resembles limonite with growth zones, enriched in Ni and in some places in Sn, was found in MFb1. While the Ni-rich Fe oxides could be explained by weathering of Ni bearing metal (as documented, e.g., in the Wabar crater [42]) or sulfide, the presence of Sn makes such a simple explanation problematic (although Sn-rich cosmic dust is also known [44]).

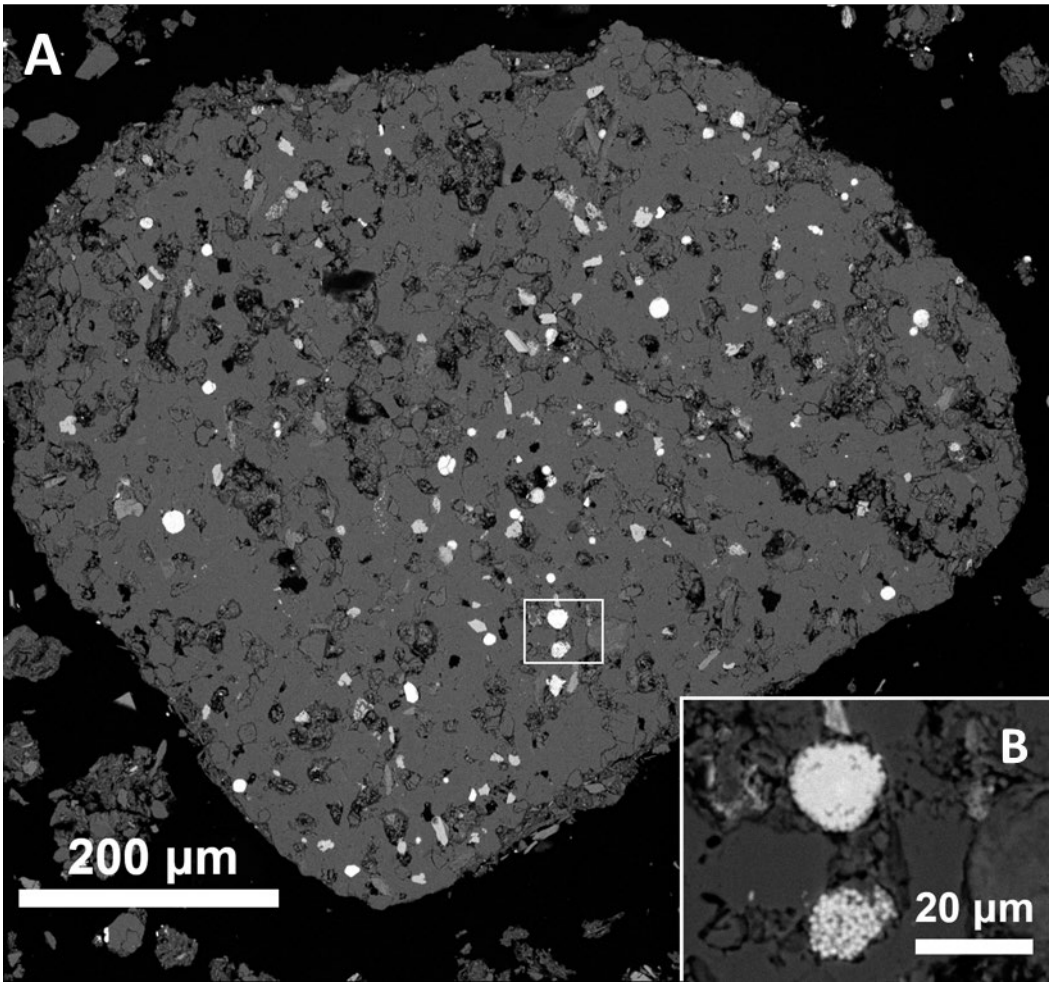

Figure 10. (**A**) Fine quartz (medium grey), Fe oxide (white), rutile (light grey), and silicates (slightly brighter than quartz): possibly thermally sintered or impact-compacted aggregate. (**B**) A detail showing that the Fe oxide particles are usually oxidized pyrite framboids, excluding identification of the object as a clast of metamorphic or magmatic rock.

3.2.2.7. Quantification of the Meteoritic Material and Spherules in MF

Mineral particles form 18 % of the "thin" sample surface and 32 % of the "thick" sample surface of MFa. This difference can be explained by the loss of larger mineral grains from the thinner section. The total scanned area (neglecting the epoxy resin and purely organic contaminants) was 4.4 cm^2.

 doi:10.20944/preprints202403.1621.v1

The area of unmelted meteorite fragment is ca. $3.15 \cdot 10^{-5}$ cm^2. And that of the largest remelted meteorite fragment (Figure 3) is ca. $5 \cdot 10^{-4}$ cm^2. All the probable meteorite fragments together occupy ca. $2 \cdot 10^{-3}$ cm^2, i.e., at most 0.05 modal %, and the mass proportion can be even lower due to low density of the prevailing porous glasses. Thus, in case of an achondritic projectile, it is not surprising that the contamination is not evident even in the bulk composition of MF.

Three Fe oxide spherules were found in the two sections of MFa which represent less than 0.1 g of material. In case that no other spherule would be found, the magnetic fraction would contain > 30 Fe oxide spherules per gram, implying > 300 per kilogram of the bulk < 2mm fraction.

3.3. Origin and Fate of the Meteoritic Matter

3.3.1. Classification of the Impactor and Comparison to Regional Meteorites

3.3.1.1. Mineralogical Features

The relatively small amount of metallic phase points to an achondrite. This could also explain the probably low content of HSE, which is mainly controlled by the amount of metal in meteorite (e.g., [45]). However, due to coarse-grained and brecciated domains in many meteorites, the modal composition of the only well-preserved sample can be little representative. The mineral chemistry is most relevant, and below we briefly discuss its comparability with major well-defined groups of meteorites (see [46,47]).

The most common meteorite falls are ordinary chondrites. The ordinary (as well as carbonaceous) chondrites have more ferrous representative composition of pyroxene – usually bronzite to hypersthene, i.e., enstatite varieties with 10-50% of the $FeSiO_3$ endmember (compare to 2-3% in the meteorite found), and olivine is usually more ferrous as well. The only chondrites with comparable composition of pyroxene are enstatite chondrites (EL and EH). They may contain many exotic mineral species characteristic for extremely reducing conditions, like silicides, nitrides, and sulfides rich in lithophile elements [48]. Regarding the differences in chemistry of minerals we found, enstatite in EL is usually extremely poor in Fe (< 1 % of the ferrosilite component [49]), while kamacite in EH is rich in Si (about 3 wt.% [48]). In addition, plagioclase in enstatite chondrites is mainly albitic which is also related to Ca content in sulfides.

Regarding achondrites, the only enstatite-rich group (also termed ‘enstatite achondrites’) are aubrites. They contain much less metal than enstatite chondrites, but otherwise they have similar contrasting features, especially very pure enstatite and forsterite, and high content of lihophile elements in sulfides; plagioclase is again albitic [50]. Regarding opaque minerals, the Ca-rich reaction rims of sulfide and kamacite in the meteorite found (Figure 2E) could reflect some loss of Ca from original sulfides, which in such a case may have been more similar to known types of enstatite-rich meteorites. In addition, it can be speculated that slightly oxidizing alteration liberated some amount of Fe, Ca and Si from the opaque minerals (see [47]), which modified the composition of silicates and formed silica. The co-occurrence of forsterite and free silica implies some disequilibrium, but enstatite chondrites commonly contain minor amounts of tridymite, cristobalite, or quartz.

Basic plagioclase is common in the most abundant achondrites – HED, which however contain relatively Fe-rich pyroxene [46], and in other groups with totally different mineralogy (angrites, lunar meteorites). The term ‘primitive enstatite achondrites’ [51] was suggested for several groups where the content of Ca-poor orthopyroxene is rather minor, and their plagioclase is again albitic.

Interestingly, Ni-rich pyrrhotite is common mainly in the interplanetary dust, which, however, usually has only submicron-sized grains of primary silicates [52].

3.3.1.2. Unusual Impactor Rich in Iron Silicides?

Several authors suggested impact of a body containing Fe silicides which were found at many places in the region [53]. Regarding the ‘iron silicon’ (silicide?) included in glass coating of a pebble from Crater No. 4, presented by [9] with a photograph from stereomicroscope, it is unclear how these authors identified the mineral. The authors [53] stated that silicides, mainly xifengite and gupeiite,

 doi:10.20944/preprints202403.1621.v1

were found in the region even more than 20 cm below the undisturbed forest soil surface, or in such archaeological situations which would preclude recent industrial origin. Other authors, however, denied the preferential occurrence of silicides in craters as well as their presence in deeper soil horizons, and pointed to the chemical and isotopic compositions and large particle size inconsistent with cosmic origin of the silicides [54,55].

However, the possibility that iron from the projectile could react with silica to form native silicon and even silicides cannot be excluded (see also [56]).

3.3.2. Micrometeorites or Contamination from Other Fall Only?

The small volume of meteoritic material found may lead to speculations that it could only represent micrometeorites or fragments of other meteorites (fallen far away). We can exclude any comparison to other known meteorites in the region (with possible exception of Fe oxide ablation spherules). Three relatively near meteorite falls were documented (ca. 25-35 km from Emmerting): Massing (Mässing) – howardite (i.e., a HED meteorite), and Mauerkirchen (in Austria) and Stubenberg – both ordinary chondrites (see [57]). As discussed above, the mineralogy and mineral chemistry of such meteorites is incomparable to the enstatite-rich meteorite found. In addition, the Stubenberg chondrite fell as late as in 2016, after we had collected the fine crater-filling sample. The closest enstatite-rich meteorite fall documented was the enstatite chondrite Neuschwanstein in 2002 at a distance of ca. 160 km [57].

The non-melted fragment is not small enough to be decelerated sufficiently in the upper atmosphere to avoid ablation, which would require a mass smaller than 10^{-12} to 10^{-10} g, only exceptionally up to 10^{-7} g; [58,59]. Thus the missing ablation features show that the body must have been larger prior to entering the atmosphere. Theoretically, it may have still been a micrometeorite only, but this would not explain the Mg-rich glasses. First, nearly pure Mg-silicates are difficult to melt by frictional heating during atmospheric passage [47]; nevertheless the meteorite surface should be also rounded by non-thermal sputtering [59]. Second, the objects found have no zoning with unmelted interior; instead, they seem to have been individual droplets. Due to chemical similarity of the porous Mg-rich glasses to the crystalline meteorite fragment, it is logic that they formed by melting of the most heated parts of the body after impact. Note that the fall did not have to be instant: some objects may have been more decelerated and arrived later. This holds for both the Fe oxide spherules (if they formed by meteorite ablation) and the unmelted fragment. Impacting bodies with highly different velocities do not have to be dispersed in large area, as shown for the Kamil crater [60]. In the case of a subvertical impact, the dispersal would be even smaller.

3.3.3.‘. Rubble Pile’ Impactor?

The fragmentation of a single body as suggested by [53] and [12] to explain the elongate “Chiemgau-Impact strewn field” is problematic (see also [55]). Nevertheless, a smaller strewn field at Burghausen, including both craters at Emmerting [7,61], may be realistic, especially in the case of a ‘rubble-pile’-like impactor. The assumption that many small asteroids have such a “loose” consistence has been confirmed by spacecraft missions (e.g., [62]).

3.3.4. Reasons for Insignificant Impactor Contamination of Crater Filling

The mass of the projectile is related to its kinetic energy, however, we know neither the impact energy, nor velocity. It can be expected that the energy necessary was larger than for a crater of similar size in a compact and even in a sandy target. The porosity significantly reduces pressure and the compression of pore space leads to a greater temperature enhancement, implying that more energy is needed to form a crater of the same size in a more porous target (e.g., [63]). While in sands and sandstones the porosity can locally enhance the pressure at grain rims [3,43], it is uncertain whether this would be significant in the coarse-grained target at Emmerting. Experiments [43] showed that local melting in sandstone begins at the shock pressure as low as 5 GPa. In addition, melting could

 doi:10.20944/preprints202403.1621.v1

have been facilitated by thermal radiation of the projectile, especially in the case of subvertical impact when the energy would not be dispersed in a large area.

Another factor which contributed to dilution and dispersal of the meteoritic contamination was the partial removal of the fine filling fraction. It may have happened during the impact by the effects of gas pressure (due to explosion, evaporation, and fire of organic matter). The authors [64] showed that the escape of vaporized pore water removed preferentially fine particles from pipes in sandstones in the Bunte Breccia at the Ries crater at the contact with hot suevite. Experimental cratering in a sandstone showed that ejecta from a wet target are finer-grained than those from a dry target [65] which also points to importance of vapor. In addition, the fine-grained filling must have been influenced by soil formation and transport of fine particles (by groundwater, gravity, and bioturbation) in the space between individual pebbles all the time after the crater formation.

Isotopic analyses of glasses could confirm a minor contamination (in the order of several %) of those melts which were exposed during the crater formation. According to [2], contamination with achondritic projectile can only be evidenced by anomalous Cr isotope ratios due to the low PGE content in achondrites.

A more exact modelling and quantification of the contamination would only be possible in the case of uncovering the crater floor and obtaining more samples from greater depths. This should be a priority of the future research, however, it has not been permitted so far.

3.4. Origin of Spherules

Spherules are commonly searched for as a marker of distal impact ejecta. Although most spherule types cannot prove an impact ([2] and references therein), enrichment in spherules is common in stratigraphic horizons with known or probable impact/airbursts events, like the Young Dryas boundary [66]. The most common spherules found in such horizons are formed by Fe oxides. Although obtaining the background abundance of spherules at distal sites in fine-grained sediments is difficult (in many such samples no spherules have been found), the minimum of 300 Fe oxide spherules/kg in MFa (not including oxidized pyrite framboids) is definitely much higher than common content in preindustrial sediments [66,67]. In (sub)recent sediments caution is needed, but the spherules found are too large for an efficient transport from relevant pollution sources (mainly large coal-combusting devices). Note that a true diameter of each spherule is quite probably higher than the diameter observed in a random section.

Spherule findings can also be important at proximal sites. The hollow Fe oxide ablation spherules related to known iron meteorite falls are usually enriched in Ni [68]. Thus, the Ni-poor spherules at Bajada del Diablo with up to 0.3 mm in diameter [39] may indicate that those craters also formed by impacts of stone meteorites.

3.5. A Preliminary Model of Crater Formation

Based on the observation presented here and in [15], we can outline the following conceptual model of the crater-forming processes at Emmerting:

1. A thermal wave from the radiation of the projectile, perhaps arriving subvertically, ignites the surface biomass and leaf litter (see also [69]).

2. The surface biomass (partly burning) and soil are pushed by the pressure wave; pressure and temperature increase below the ground as well. By interaction of organic matter with groundwater at high temperature and elevated pressure, a fluid forms which is rich in K, Na, Cu (Rb, Ca, Mg, Mn), and K-rich surface glasses begin to form.

3. Melting and explosion of the main projectile body (perhaps slightly above the ground – depending on the compressed air pressure), perhaps colliding with the onset of vapor expansion which makes it difficult to delimit the compression and excavation phase. The excavation phase is relatively limited (as compared to common craters) due to mutual collisions of pebbles (see also [14]). The collisions lead to complicated relations of melting and deformation, and make the heating of pebble interior possible (heating by plastic deformation was also documented for experimental projectiles [70]). Ejecting is limited and downward transport of fine particles and fragments is

 doi:10.20944/preprints202403.1621.v1

significant (as supposed for highly porous targets, like some asteroids [71]), probably leading to formation of the compact body below the crater floor indicated geophysically [16].

4. The molten meteorite fragments solidify to glass, influenced by the K and Ca-rich fluids (later ablation spherules and unmelted to slightly melted meteorite material arrives). Welding (limited) and cooling of pebbles start. The cooling is relatively slow for several reasons: i) many pebbles have been heated inside, ii) after water evaporation, fire from organic matter has persisted for some time, iii) cooling effect of liquid water which reached the site soon after the crater formation would be prevented by its exothermic reaction with quicklime burned from carbonates.

5. Conclusions

The impact origin of the Crater No. 4 at Emmerting is the only realistic explanation of the meteorite finding and other phenomena (see also [15]), although some details of the crater-forming process in such a porous but very coarse target remain to be clarified. The projectile was dominated by clinoenstatite and contains typical meteoritic minerals (kamacite, relict troilite, possibly merrillite). Remelted fragments of the same meteorite are more common and consist mainly of Mg-rich glass. The meteoritic contamination is little contrasting, leaving no unequivocal chemical or Os-isotope signature in the bulk crater filling (at least in small depths). This can be explained by differentiated achondritic composition of the projectile and small portion of the original fine filling fraction in the present crater.

Some of the hollow spheroid particles, including relatively large Fe oxide spherules, are chemically equivalent to small impact spherules of distal sites, and possibly to impact spherules in craters formed by stone meteorites.

In the Crater No. 5, even lower amount of meteoritic material can be expected. Elevated contents of several metals in the filling can be rather explained by the influence of recent stream sediments. The extreme deformation and fracturing of pebbles, including melt injections into thin fractures in quartz and zircon [15], and the proximity of the Crater No. 4 are the main evidence for the impact origin of Crater No. 5.

Supplementary Materials: The following supporting information can be downloaded at: www.mdpi.com/xxx/s1, Figure S1: TGA results; Tables S1-3: Complete results of chemical analyses.

Author Contributions: Conceptualization, V.P., P.K. and J.M.; methodology, V.P., P.M. and T.T.; investigation, V.P., P.K., L.T., P.M., T.T., R.Š., J.A. and P.Š.; resources, V.P., P.K. and L.T.; data curation, V.P. and J.M.; writing—original draft preparation, V.P., P.K. and G.K.; writing—review and editing, V.P., J.M. and G.K.; visualization, V.P., J.A. and J.M.; supervision, V.P.; project administration, V.P.; funding acquisition, T.T., P.M. and J.M. All authors have read and agreed to the published version of the manuscript.

Funding: The work was funded by the Ministry of Education, Youth and Sports of the Czech Republic within the projects LM2023073 (The VR-1 Nuclear Experimental Hub), LM2015056 (CANAM infrastructure), LM2023041 (CICRR infrastructure), and RVO: 68145535 (project for the long-term conceptual development of research organizations at the Institute of Geonics).

Data Availability Statement: The data presented in the tables and figures or elsewhere are openly available as the Supplementary Materials or on request from the corresponding author.

Acknowledgments: We thank to Marek Dosbaba (TESCAN) who performed the automatic scanning with TIMA analyzer, and to František Laufek for performing XRD analyses.

Conflicts of Interest: The authors declare no conflict of interest.

References

1. Osinski, G.R.; et al. Impact Earth: A review of the terrestrial impact record. *Earth Sci. Rev.* **2022**, *232*, 104112. https://doi.org/10.1016/j.earscirev.2022.104112
2. French, B.M.; Koeberl, C. The convincing identification of terrestrial meteorite impact structures: what works, what doesn't, and why. *Earth Sci. Rev.* **2010**, *98*, 123–170. https://doi.org/10.1111/maps.13657
3. Güldemeister, N.; Durr, N.; Wünnemann, K.; Hiermaier, S. Propagation of impact-induced shock waves in porous sandstone using mesoscale modeling. *Meteorit. Planet. Sci.* **2013**, *48*, 115–133. https://doi.org/10.1111/j.1945-5100.2012.01430.x

4. Fazio, A.; D'Orazio, M.; Cordier, C.; Folco, L. Target–projectile interaction during impact melting at Kamil Crater, Egypt. *Geochim. Cosmochim. Acta* **2016**, *180*, 33–50. https://doi:10.1016/j.gca.2016.02.003
5. Tancredi, G. et al. A meteorite crater on Earth formed on September 15, 2007: The Carancas hypervelocity impact. *Meteorit. Planet. Sci.* **2009**, *44*, 1967–1984. https://doi.org/10.1111/j.1945-5100.2009.tb02006.x
6. Jull, A.J.T. 2001. Terrestrial ages of meteorites. In: Peucker-Ehrenbrink B.; Schmitz B. (Eds.), Accretion of extraterrestrial matter throughout Earth's history. Springer US, Boston, pp. 241-266. https://doi.org/10.1007/978-1-4419-8694-8_14
7. Fehr, K.T.; Pohl, J.; Mayer, W.; Hochleitner, R.; Faßbinder, J.; Geiß, E.; Kerscher, Y. A meteorite impact crater field in eastern Bavaria? A preliminary report. *Meteorit. Planet. Sci.* **2005**, *40*, 187–194. https://doi.org/10.1111/j.1945-5100.2005.tb00374.x
8. Schüssler, U. Chiemgau-Impakt: Petrographie und Geochemie von Geröllen mit Deformationsmerkmalen und starker thermischer Beanspruchung aus dem nördlichen Bereich des Impakt-Areals. Chiemgau Impact Research Team, 2005. Available online: http://www.chiemgau-impact.com/wp-content/uploads/2011/08/Petrographie-und-Geochemie.pdf (accessed on 18 October 2023).
9. Rösler, W.; Patzelt, A.; Hoffmann, V.; Raeymaekers, B. Characterization of a small crater-like structure in S.E. Bavaria, Germany. In Proceedings of the First International Conference on Impact Cratering in the Solar System, Noordwijk, Netherlands, 8-12 May 2006. Available online: https://sci.esa.int/documents/33321/35974/1567255423911-ESLAB40-Proc_295499-Roesler.pdf (accessed on 18 October 2023).
10. Doppler, G.; Geiss, E. Der Tüttensee im Chiemgau - Toteiskessel statt Impaktkrater. Bayerisches Landesamt für Umwelt, 2005. Available online: https://www.lfu.bayern.de/geologie/meteorite/bayern/doc/tuettensee.pdf (accessed on 18 October 2023).
11. Darga, R.; Wierer, J.F. (2009): Der Chiemgau-Impakt - eine Spekulationsblase - Oder: Der Tüttensee ist KEIN Kometenkrater. In Auf den Spuren des Inn-Chiemsee-Gletschers - Exkursionen. S. 174-185. München (Pfeil) 2009, ISBN 978-3-89937-104-8. Available online: http://www.scribd.com/doc/26218026/Der-Chiemgau-Impakt-eine-Spekulationsblase-Oder-Der-Tuttensee-ist-KEIN-Kometenkrater (accessed on 20 March 2024).
12. Ernstsson, K.; Mayer, W.; Neumair, A.; Rappenglück, B.; Rappenglück, M.A.; Sudhaus, D.; Zeller, K.W. The Chiemgau crater strewn field: evidence of a Holocene large impact event in southeast Bavaria, Germany. *J. Sib. Fed. Univ. - Eng. Technol.* **2010**, *1*, 72–103. Available online: https://core.ac.uk/download/pdf/38633216.pdf (accessed on 17 October 2023).
13. Procházka, V.; Martinec, P.; Štorc, R.; Kalenda, P.; Thinová, L.; Tengler, R.; Mizera, J. Holocene impact crater at Emmerting (Bavaria): mineralogy of the filling including meteorite and a possible explanation of the compact body below the crater bottom. In Proceedings of the 27th Quaternary Seminary Meeting, Brno, Czech Republic, 2 December 2022. In Czech, available online: https://www.researchgate.net/publication/368358601 (accessed on 18 October 2023).
14. Procházka, V. Melt behavior in two impact craters at Emmerting, Germany: Deformation, expansion, injections, and the role of underpressure and mutual collisions of pebbles. In Proceedings of the 54th Lunar and Planetary Science Conference, The Woodlands, TX, USA, 13–17 March 2023. Available online: https://www.hou.usra.edu/meetings/lpsc2023/pdf/2102.pdf (accessed on 18 October 2023).
15. Procházka, V.; Herrmann, H.; Kalenda, P.; Martinec, P.; Mizera, J.; Trojek, T.; Thinová, L.; Kletetschka G.; Adámek, J.; Souček, K. Comparison of Melting-Affected Rocks from Presumed Small Impact Craters and Old Limekilns in Bavaria, Germany. *Preprints* **2024**, 2024031373 (submitted to Minerals, ID minerals-2947833) https://www.preprints.org/manuscript/202403.1373/v1
16. Kalenda, P.; Thinová, L.; Tengler, R.; Procházka, V.; Mizera, J. Martinec, P.; Kletetschka G.; Trojek T. Two impact craters at Emmerting, Germany: Field documentation and geophysics. *Geodynamics* **2024** (in press).
17. Strnad, L.; Mihaljevič, M.; Šebek, O. Laser ablation and solution ICP-MS determination of REE in USGS BIR-1G, BHVO-2G and BCR-2G glass reference materials. *Geostand. Geoanal. Res.* **2005**, *29*, 303–314. https://doi.org/10.1111/j.1751-908X.2005.tb00902.x
18. Řanda, Z.; Frána, J.; Mizera, J.; Kučera, J.; Novák, J. K.; Ulrych, J.; Belov, A. G.; Maslov, O. D. Instrumental neutron and photon activation analysis in the geochemical study of phonolitic and trachytic rocks. *Geostand. Geoanal. Res.* **2007**, *31*, 275–283. https://doi.org/10.1111/j.1751-908X.2007.00839.x
19. Mizera, J.; Řanda, Z. Instrumental neutron and photon activation analyses of selected geochemical reference materials. *J. Radioanal. Nucl. Chem.* **2010**, *284*, 157–163. https://doi.org/10.1111/j.1751-908X.2007.00839.x
20. Mizera, J.; Havelcová, M.; Machovič, V.; Borecká, L.; Vörös, D. Neutron activation analysis in urban geochemistry: Impact of traffic intensification after opening the Blanka Tunnel Complex in Prague. *Minerals* **2022**, *12*, 281. https://doi.org/10.3390/min12030281
21. Topuz, G.; Hegner, E.; Homam, S. M.; Ackerman, L.; Pfänder, J. A.; Karimi, H. Geochemical and geochronological evidence for a Middle Permian oceanic plateau fragment in the Paleo-Tethyan suture zone of NE Iran. *Contrib. Mineral. Petrol.* **2018**, *173*, Art. No. 81. https://doi.org/ 10.1007/s00410-018-1506-x

22. Hrstka, T; Gottlieb, P; Breiter, K.; Skála, R.; Motl, D. Automated mineralogy and petrology - applications of TESCAN Integrated Mineral Analyzer (TIMA). *J. Geosci.* **2018**, *63*, 47–63. https://doi.org/10.3190/jgeosci.250
23. Fischer-Gödde, M.; Becker, H.; Wombacher, F. Rhodium, gold and other highly siderophile element abundances in chondritic meteorites. *Geochim. Cosmochim. Acta* **2010**, *74*, 356–379. https://doi.org/10.1016/j.gca.2009.09.024
24. Hart, S.R.; Ravizza, G.E. Os partitioning between phases in lherzolite and basalt. *Geophys. Monogr.* **1996**, *95*, 123–134. https://doi.org/10.1029/GM095p0123
25. Brenan, J.M.; Finnigan, C.F.; McDonough, W.F.; Homolova, V. Experimental constraints on the partitioning of Ru, Rh, Ir, Pt and Pd between chromite and silicate melt: The importance of ferric iron. *Chem. Geol.* **2012**, *302–303*, 16C32. https://doi.org/ 10.1016/j.chemgeo.2011.05.015
26. Walker, R.J.; Prichard, H.M.; Ishiwatari, A.; Pimentel, M. The osmium isotopic composition of convecting upper mantle deduced from ophiolite chromites. *Geochim. Cosmochim. Acta* **2002**, *66*, 329–345. https://doi.org/ 10.1016/S0016-7037(01)00767-0
27. Mindat Database. Hudson Institute of Mineralogy, Keswick, USA. www.mindat.org (accessed on 24 February 2024).
28. Gasparik, T. System MgO-SiO_2. In Phase Diagrams for Geoscientists, pp. 13–31. Springer, Berlin, Heidelberg **2003**. https://doi.org/10.1007/978-3-540-38352-9_2
29. Folco, L.; Mellini, M. Enstatite chemical composition and microstructures in the La Villa H4 chondrite. *Meteorit. Planet. Sci.* **2000**, *35*, 733–742. https://doi.org/10.1111/j.1945-5100.2000.tb01457.x
30. Rubin, A.E. Impact features of enstatite-rich meteorites. *Chem. Erde* **2015**, *75*, 1-28. https://doi.org/10.1016/j.chemer.2014.09.001
31. Wozniakiewicz, P. J. et al. (10 co-authors). Investigation of iron sulfide impact crater residues: A combined analysis by scanning and transmission electron microscopy. *Meteorit. Planet. Sci.* **2011**, *46*, 1007–1024. https://doi.org/ 10.1111/j.1945-5100.2011.01206.x
32. Ebert, M.; Hecht, L.; Deutsch, A.; Kenkmann, T. Chemical modification of projectile residues and target material in a MEMIN cratering experiment. *Meteorit. Planet. Sci.* **2013**, *48*, 134–149. https://doi.org/10.1111/j.1945-5100.2012.1429.x
33. Hörz, F.; Mittlefehldt, D. W.; See, T. H.; Galindo, C. Petrographic studies of the impact melts from Meteor Crater, Arizona, USA. *Meteorit. Planet. Sci.* **2002**, *37*, 501–531. https://doi.org/10.1111/j.1945-5100.2002.tb00836.x
34. Schmitt, W.; Palme, H.; Wänke, H. Experimental determination of metal/silicate partition coefficients for P, Co, Ni, Cu, Ga, Ge, Mo, and W and some implications for the early evolution of the Earth. *Geochim. Cosmochim. Acta* **1989**, *53*, 173–185. https://doi.org/10.1016/0016-7037(89)90284-6
35. Mittlefehldt, D. W.; See, T. H.; Hörz, F. Dissemination and fractionation of projectile materials in the impact melts from Wabar crater, Saudi Arabia. *Meteoritics* **1992**, *27*, 361–370. https://doi.org/10.1111/j.1945-5100.1992.tb00217.x
36. Schmitz, B.; Tassinari, M.; Peucker-Ehrenbrink, B. A rain of ordinary chondritic meteorites in the early Ordovician. *Earth Planet. Sci. Lett.* **2001**, *194*, 1–15. https://doi.org/ 10.1016/S0012-821X(01)00559-3
37. Procházka, V.; Trojek, T. XRF- and EMP- investigation of glass coatings and melted domains of pebbles from craters in Chiemgau, Germany. In Proceedings of the 48th Lunar and Planetary Science Conference, The Woodlands, TX, USA, 20–24 March 2017. Available online: https://www.hou.usra.edu/meetings/lpsc2017/pdf/2401.pdf (accessed on 18 October 2023).
38. Bowen, N.L., Tuttle, O.F. The system MgO-SiO_2-H_2O. *Geol. Soc. Am. Bull.* **1949**, *60*, 439–460.
39. Orgeira, M.J. et al. Extraterrestrial microspherules from Bajada del Diablo, Chubut, Argentina. *Geosci. Frontiers* **2017**, *8*, 137–149. https://doi.org/ 10.1016/j.gsf.2016.01.004
40. Bau, M.; Koschinsky, A. Oxidative scavenging of cerium on hydrous Fe oxide: evidence from the distribution of rare earth elements and yttrium between Fe oxides and Mn oxides in hydrogenetic ferromanganese crusts. *Geochem. J.* **2009**, *43*, 37–47. https://doi.org/ 10.2343/geochemj.1.0005
41. GESTIS Database. Institut für Arbeitsschutz, Germany. GESTIS Substance Database (dguv.de) (accessed on 10 February 2024).
42. Gnos, E. et al. The Wabar impact craters, Saudi Arabia, revisited. *Meteorit. Planet. Sci.* **2013,** *48*, 2000–2014. https://doi.org/10.1111/maps.12218
43. Kowitz, A.; Güldemeister, N.; Reimold, W.U.; Schmitt, R.T.;Wünnemann, K. Diaplectic quartz glass and SiO_2 melt experimentally generated at only 5 GPa shock pressure in porous sandstone: laboratory observations and meso-scale numerical modeling. *Earth Planet. Sci. Lett.* **2013**, *384*, 17–26. https://doi.org/10.1016/j.epsl.2013.09.021
44. La Violette, P.A. The episodic influx of tin-rich cosmic dust particles during the last ice age. *Adv. Space Res.* **2015**, *56*, 2402–2427. https://doi.org/ 10.13140/RG.2.1.3182.1525
45. Casanova, I.; Keil, K.; Newsom, H.E. Composition of metal in aubrites: constraints on core formation. *Geochim. Cosmochim. Acta* **1993**, *57*, 675–682. https://doi.org/ 10.1016/0016-7037(93)90377-9

46. Davis, A.M. (Ed.) Meteorites, comets, and planets; Treatise on Geochemistry, vol. 1. Elsevier, Amsterdam, 2005. ISBN 9780080525358
47. Rubin, A.E.; Ma, C. Meteoritic minerals and their origins. *Chem. Erde* **2017**, 77, 325–385. https://doi.org/10.1016/j.chemer.2017.01.005
48. Keil, K. Mineralogical and chemical relationships among enstatite chondrites. *J. Geophys. Res.* **1968**, *73*, 6945–6976. https://doi.org/ 10.1029/JB073i022p06945
49. Wasson, J.T.; Kallemeyn, G.W.; Rubin, A.E. Equilibration temperatures of EL chondrules: a major downward revision in the ferrosilite contents of enstatite. *Meteoritics* **1994**, *29*, 658–662. https://doi.org/10.1111/j.1945-5100.1994.tb00781.x
50. Watters, T.R.; Prinz, M. Aubrites: Their origin and relationship to chondrites. *Proc. Lunar Planet. Sci. Conf. 10th* **1979**, *10*, 1073–1093. Available online: https://repository.si.edu/bitstream/handle/10088/6405/197905.pdf (accessed on 20 March 2024).
51. Pilski, A.S.; Przylibski, T.A.; Łuszczek, K. Primitive enstatite achondrites. Meteorites **2011**, *0*, 9–21. Available online: http://www.meteorites.pwr.wroc.pl/issues/0/meteorites00-02.pdf accessed on 20 March 2024).
52. Bradley, J.P. Interplanetary Dust Particles. In Meteorites, comets, and planets (Treatise on Geochemistry, vol. 1.); Davis, A.M. (Ed.), Meteorites, Comets, and Planets, Elsevier, Amsterdam, **2005**, pp. 689-712, ISBN 9780080525358.
53. Rappenglück, M.A.; Ernstson, K.; Mayer, W.; Beer, R.; Benske, G.; Siegl, C., Sporn, R.; Bliemetsrieder, T.; Schüssler, U. The Chiemgau impact event in the Celtic Period: evidence of a crater strewnfield and a cometary impactor containing presolar matter. Available online: https://www.chiemgau-impakt.de/pdfs/Chiemgau_impact.pdf (accessed on 17 October 2023).
54. Fehr, K.T.; Hochleitner, R.; Hölzl, S.; Geiss, E.; Pohl, J.; Faßbinder, J. Ferrosilizium-Pseudometeorite aus dem Raum Burghausen, Bayern. *Der Aufschluß* **2004**, *55*, 297–303.
55. Heinlein, D. Der so genannte „Kelten-Killer-Komet" – gab es einen Kometeneinschlag im Chiemgau? *Zeitschrift der Vereinigung der Sternfreunde* **2009**, *30*, 84–86.
56. Anand, M.; Taylor, L.A.; Nazarov, M.A.; Shu, J.; Mao, H.-K.; Hemley, R.J.: Space weathering on airless planetary bodies: clues from the lunar mineral Hapkeite, *Proc. Nat. Acad. Sci.* **2004**, *101*, 6847–6851. https://doi.org/10.1073/pnas.0401565101
57. Meteoritical Bulletin Database. International Society for Meteoritics and Planetary Science. https://www.lpi.usra.edu/meteor/metbull.php (accessed on 30 January 2024).
58. Plane, J.M.C. Cosmic dust in the earth's atmosphere. *Chem. Soc. Rev.* **2012**, *41*, 6507–6518. https://doi.org/10.1039/c2cs35132c
59. Vondrak, T.; Plane, J. M. C.; Broadley, S.; Janches, D. A chemical model of meteoric ablation. *Atmos. Chem. Phys. Discuss.* **2008**, *8*, 7015–7031. https://doi.org/10.5194/acp-8-7015-2008
60. D'Orazio, M.; Folco, L.; Zeoli, A.; Cordier, C. Gebel Kamil: The iron meteorite that formed the Kamil crater (Egypt). *Meteorit. Planet. Sci.* **2011**, *46*, 1179–1196. https://doi.org/10.1111/j.1945-5100.2011.01222.x
61. Hoffmann, V.; Rösler, W.; Schibler, L. Anomalous magnetic signature of top soils in Burghausen area, SE Germany. *Geophys. Res. Abstr.* **2004**, *6*, 5041.
62. Fujiwara, A. et al. (21 co-authors). The rubble-pile asteroid Itokawa as observed by Hayabusa. *Science* **2006**, *312*, 1330–1334. https://doi.org/10.1126/science.1125841
63. Love, S.G.; Hörz, F.; Brownlee, D.E. Target porosity effects in impact cratering and collisional disruption. *Icarus* **1993**, *105*, 216–224. https://doi.org/10.1006/icar.1993.1119
64. Pietrek, A.; Kenkmann, T. Ries Bunte Breccia revisited: Indications for the presence of water in Itzing and Otting drill cores and implications for the emplacement process. *Meteorit. Planet. Sci.* **2016**, *51*, 1203–1222. https://doi.org/10.1111/maps.12656
65. Buhl, E.; Poelchau, M. H.; Dresen, G.; Kenkmann, T. Deformation of dry and wet sandstone targets during hypervelocity impact experiments, as revealed from the MEMIN Program. *Meteorit. Planet. Sci.* **2013**, *48*, 71–86. https://doi.org/10.1111/j.1945-5100.2012.01431.x
66. Wittke J.H. et al. Evidence for deposition of 10 million tonnes of impact spherules across four continents 12,800 y ago. *Proc. Nat. Acad. Sci.* **2013**, *110*, E2088-E2097. https://doi.org/10.1073/pnas.1301760110
67. Kletetschka G. et al. Cosmic impact event in lake sediments from central Europe postdates the Laacher See eruption and marks onset of the Younger Dryas. *J. Geol.* **2018**, *126*, 561–575. https://doi.org/10.1086/699869
68. Badyukov, D.D.; Raitala, J. Ablation spherules of the Sikhote Alin meteorite and their genesis. *Petrology*, **2012**, *20*, 520–528. https://doi.org/ 10.1134/S086959111206001X
69. Řanda, Z.; Mizera, J.; Frána, J.; Kučera, J. Geochemical characterization of moldavites from a new locality, the Cheb Basin, Czech Republic. *Meteorit. Planet. Sci.* **2008**, *43*, 461–477. https://doi.org/10.1111/j.1945-5100.2008.tb00666.x
70. Kenkmann, T.; Trullenque, G.; Deutsch, A.; Hecht, L.; Ebert, M.; Salge, T.; Schäfer, F.; Thoma, K. Deformation and melting of steel projectiles in hypervelocity cratering experiments. *Meteorit. Planet. Sci.* **2013**, *48*, 150–164. https://doi.org/10.1111/maps.12018

 doi:10.20944/preprints202403.1621.v1

71. Housen K.R., Sweet W.J., Holsapple K.A. Impacts into porous asteroids. *Icarus* **2018**, *300*, 72–96. https://doi.org/ 10.1016/S0019-1035(03)00024-1